Key Points:
- Global wave hindcasts using the observation-based source terms are developed and validated against extensive observations
- The wave hindcasts show promising performance across multiple parameters, including wave height, period, and high-order spectral moments
- Intercomparisons of wave height from the hindcast, buoys, and altimeters highlight the inconsistency and inhomogeneity in these data sets

Correspondence to:
A. V. Babanin,
a.babanin@unimelb.edu.au

Global Wave Hindcasts Using the Observation-Based Source Terms: Description and Validation

Qingxiang Liu[1,2] , Alexander V. Babanin[2,3], W. Erick Rogers[4] , Stefan Zieger[5], Ian R. Young[2], Jean-Raymond Bidlot[6] , Tom Durrant[7] , Kevin Ewans[8], Changlong Guan[1], Cagil Kirezci[2], Gil Lemos[9], Keith MacHutchon[10], Il-Ju Moon[11] , Henrique Rapizo[12], Agustinus Ribal[13] , Alvaro Semedo[14] , and Juanjuan Wang[15]

[1]Physical Oceanography Laboratory, Ocean University of China, Qingdao, China, [2]Department of Infrastructure Engineering, University of Melbourne, Melbourne, VIC, Australia, [3]Laboratory for Regional Oceanography and Numerical Modeling, National Laboratory for Marine Science and Technology, Qingdao, China, [4]Naval Research Laboratory, Stennis Space Center, MS, USA, [5]Bureau of Meteorology, Melbourne, VIC, Australia, [6]European Centre for Medium-Range Weather Forecasts, Reading, UK, [7]Oceanum Ltd, Raglan, Waikato, New Zealand, [8]MetOcean Research Ltd, New Plymouth, New Zealand, [9]Instituto Dom Luiz, Faculty of Sciences of the University of Lisbon, Lisbon, Portugal, [10]Department of Oceanography, University of Cape Town, Cape Town, South Africa, [11]Typhoon Research Center, Jeju National University, Jeju, South Korea, [12]MetOcean Solutions, Raglan, New Zealand, [13]Department of Mathematics, Faculty of Mathematics and Natural Sciences, Hasanuddin University, Makassar, Indonesia, [14]Department of Water Science and Engineering, IHE Delft, Delft, The Netherlands, [15]National Marine Environmental Forecasting Center, Ministry of Natural Resources, Beijing, China

Abstract Global wave hindcasts are developed using the third generation spectral wave model WAVEWATCH III with the observation-based source terms (ST6) and a hybrid rectilinear-curvilinear, irregular-regular-irregular grid system (approximately at $0.25° \times 0.25°$). Three distinct global hindcasts are produced: (a) a long-term hindcast (1979–2019) forced by the ERA5 conventional winds U_{10} and (b) two short-term hindcasts (2011–2019) driven by the NCEP climate forecast system (CFS)v2 U_{10} and the ERA5 neutral winds $U_{10,neu}$, respectively. The input field for ice is sourced from the Ocean and Sea Ice Satellite Application Facility (OSI SAF) sea-ice concentration climate data records. These wave simulations, together with the driving wind forcing, are validated against extensive in-situ observations and satellite altimeter records. The performance of the ST6 wave hindcasts shows promising results across multiple wave parameters, including the conventional wave characteristics (e.g., wave height H_s and wave period) and high-order spectral moments (e.g., the surface Stokes drift and mean square slope). The ERA5-based simulations generally present lower random errors, but the CFS-based run represents extreme sea states (e.g., $H_s > 10$ m) considerably better. Novel wave parameters available in our hindcasts, namely the dominant wave breaking probability, wave-induced mixed layer depth, freak wave indexes and wave-spreading factor, are further described and briefly discussed. Inter-comparisons of H_s from the long-term (41 years) wave hindcast, buoy measurements and two different calibrated altimeter data sets highlight the inconsistency in these altimeter records arising from different calibration methodology. Significant errors in the low-frequency bins (period $T > 15$ s) for both wave energy and directionality call for further model development.

Plain Language Summary Ocean surface waves are fundamentally important for ocean engineering design, ship navigation, air-sea exchange of gas, heat, momentum and energy, upper ocean dynamics, and remote sensing of the ocean. Spectral wave modeling is an indispensable tool to estimate sea state information. In this study, we present new global wave hindcasts developed using the state-of-the-art model physics and numerics and the modern reanalysis winds and satellite sea ice records. It is demonstrated through validation against in-situ observations and altimeter records that the global wave hindcasts perform well across multiple parameters. Meanwhile, intercomparisons of wave height from the long-term hindcast, buoys, and altimeters reveal inconsistency and potential inhomogeneity in these different data sets. The wave hindcasts we developed, in combination with global wave databases published previously, will form a large ensemble of realizations of historical evolution of sea states simulated with distinct wave physics and wind forcing, which will help quantify sea states in real oceans more accurately.

1. Introduction

Wind-generated waves present at the air-sea interface are fundamentally important for ocean engineering design, ship navigation, air-sea exchange of gas, heat, momentum and energy, upper ocean dynamics, sea ice fracture and breakup, and remote sensing of the ocean (e.g., Babanin, 2011, ch. 9; Cavaleri et al., 2012; Donelan, 1990; Donelan & Pierson, 1987). Nowadays sea state information is routinely reported by moored or drifting buoys, platforms and rigs (e.g., Ardhuin et al., 2019), Voluntary Observing Ships (Gulev & Grigorieva, 2006), satellites (e.g., Hasselmann et al., 2012; Hauser et al., 2020; Zieger et al., 2009) and numerical weather forecasts using spectral wave models (e.g., Bidlot, 2017). Among these various approaches, spectral wave modeling has been playing an indispensable role in many wave-related engineering and geophysical applications. The performance of third-generation spectral wave models (e.g., Booij et al., 1999; The WAMDI Group, 1988; Tolman, 1991) has also been continuously improved over the past decades owing to upgrades in model physics, numerics and enhancement in the quality of input fields (e.g., Cavaleri et al., 2007, 2018; Janssen, 2008; Resio et al., 2019).

Compared against observational systems (e.g., buoys and satellites), spectral wave modeling is highly desired in at least two aspects. First, it is capable of providing high sampling resolution (constrained by the available computational resources) in both space and time. Second, it can yield the full information of sea states (i.e., the full directional wave spectrum) and other complemental quantities relevant for wind-wave-current interactions (e.g., air-sea momentum flux, surface Stokes drift, wave breaking statistics; Fan et al., 2009; Rascle et al., 2008; Romero, 2019, see also our Section 6) on a wide range of geophysical scales (from global to regional). While more research is needed to further improve our understanding of wind wave physics and individual source terms in wave models, previous research has clearly demonstrated that the present-day spectral wave models perform remarkably well in estimating conventional wave parameters (e.g., wave height and period) in oceanic waters which are sufficiently far from coastlines and sea ice, provided that the driving winds are sufficiently accurate (Janssen, 2008). More recently, the accuracy of the modeled high-order spectral moments (e.g., mean square slope) has also been significantly enhanced (Ardhuin et al., 2010; Liu et al., 2019) largely owing to the usage of more physical wave breaking source functions. Accordingly, short-term and long-term wave reanalyses and hindcasts forced by good-quality winds (e.g., Bidlot et al., 2019; Chawla et al., 2013; Fan et al., 2012; Rascle & Ardhuin, 2013) have been widely used for wave climate analysis (e.g., Semedo et al., 2011; Young et al., 2020), assessment of wave energy resources (e.g., Hemer et al., 2017; Ribal et al., 2020), investigating wind-wave interactions (e.g., Hanley et al., 2010), calculating the Stokes drift velocity profile (e.g., Breivik et al., 2014; Carrasco et al., 2014), diagnosing wave-forced turbulence in the upper ocean (e.g., Belcher et al., 2012; Thomson et al., 2016), and for calibrating and validating satellite wave measurements (e.g., Liu et al., 2016; Hauser et al., 2020), among others.

In this study, we present new global wave hindcasts developed using the third-generation spectral wave model WAVEWATCH III (hereafter WW3; The WAVEWATCH III Development Group (WW3DG) (2019), hereafter WW3DG19; version 7.00 was used with modifications for including wave parameters described in Section 6 and for fixing bugs in regridding model outputs from multiple grids). These data were built upon the observation-based source term parameterizations (ST6; Liu et al., 2019; Rogers et al., 2012; Zieger et al., 2015) and the irregular-regular-irregular (IRI) grid system (roughly 0.25° × 0.25°; Rogers & Linzell, 2018). Modern satellite sea ice data (Lavergne et al., 2019) and reanalysis winds were used as model input fields. Specifically, three global hindcasts were produced, including a long-term run (1979–2019) forced by the ERA5 conventional winds (Hersbach et al., 2020), and two short-term runs (2011–2019) forced by the NCEP climate forecast system (CFS) winds (Saha et al., 2010, 2014) and the ERA5 neutral winds (Bidlot et al., 2019), respectively. These wave hindcasts, in combination with global wave databases published previously (e.g., Bidlot et al., 2019; Chawla et al., 2013; Rascle & Ardhuin, 2013), represent realizations of historical sea state information as simulated with different wave physics packages and wind forcing, and therefore are expected to be highly useful for future climatic and engineering research.

Starting from Section 2, we will introduce the in-situ measurements and satellite altimeter observations used for model validation and comparisons, followed by the detailed description of model physics, numerics, and forcing inputs (winds, ice) in Section 3. Intercomparisons of the ERA5 and CFS winds are also presented in Section 3.3. Thorough validations of our global wave hindcasts against altimeter and buoy observations are given in Section 4 and 5, respectively. The quality of the modeled spectral shape is also

Table 1
Satellite and Reanalysis Datasets Used in This Study, Including Environmental Parameters We Selected (Significant Wave Height H_s, Wind 10 m Above the Sea Surface U_{10}, Ice Concentration c_i, 10 m Neutral Wind $U_{10,neu}$, 2 m Air Temperature T_2, Sea Surface Temperature T_s and Mixed Layer Depth h_{ml}), Data Duration, Spatial and Temporal Resolutions and Corresponding References

Data set	Parameters	Duration	Resolution	Reference
Altimeters	H_s, U_{10}	03/1985–12/2019	1 Hz, $O\,(7)$ km	Ribal and Young (2019)
Altimeters	H_s	08/1991–12/2018	monthly, $1° \times 1°$	Dodet et al. (2020)
OSI-450	c_i	01/1979–12/2015	daily, 25×25 km^2	Lavergne et al. (2019)
OSI-430-b	–	01/2016–12/2019	–	–
ERA5	$U_{10}, U_{10,neu}, c_i, T_2, T_s$	01/1979–12/2019	hourly, $0.25° \times 0.25°$	Hersbach et al. (2020)
CFSR	U_{10}	01/1979–12/2010	hourly, $0.5° \times 0.5°$	Saha et al. (2010)
CFSv2	–	01/2011–12/2019	–	Saha et al. (2014)
CCI v2.1	depth T_s	01/1982–12/2019	daily, $0.25° \times 0.25°$	Merchant et al. (2019)
Ifremer/Los	annual climatology of h_{ml}	1961–2008	monthly, $2° \times 2°$	de Boyer Montégut et al. (2004)

carefully evaluated against buoy spectra in terms of multiple spectral metrics therein. Section 6 provides further brief explanations of unconventional wave parameters available from our database and associated preliminary climatological analysis. Discussion and conclusions in Section 7 finalize this paper.

2. Satellite and In-Situ Observations

2.1. Altimeter Data Set

The calibrated and validated altimeter data set developed by Ribal and Young (2019) is adopted as the reference for evaluating the accuracy of the wind forcing and wave hindcasts on a global scale (Table 1). It consists of more than 30 years (1985–2019) of global significant wave height H_s and wind speed U_{10} from 14 radar altimeters, of which the missions and temporal coverage are illustrated in Figure 1a. The 1 Hz altimeter H_s and U_{10} records have been quality-controlled and extensively validated against in-situ buoy measurements and against remote sensing observations from other simultaneously operating altimeters. The altimeter estimates H_s from the slope of the leading edge of the returned waveform (Chelton et al., 2001) and retrieves U_{10} from the normalized radar cross section σ_0 by employing empirical algorithms (e.g., Zieger et al., 2009). The single-parameter algorithm of Abdalla (2012) was adopted in Ribal and Young (2019) to derive U_{10} with a σ_0 offset applied to each altimeter to optimize the rms error. An empirical correction proposed by Young (1993) was further introduced for U_{10} greater than 18 m s^{-1}, given by

$$U_{10} = -6.4\sigma_0 + 69. \tag{1}$$

The altimeter data are archived in 1° by 1° bins, and within each bin, full data resolution is provided with all parameters for each 1 Hz altimeter record available (e.g., time, longitude, latitude, calibrated H_s, and U_{10}). For comparison, gridded model outputs are interpolated bi-linearly in space and linearly in time to altimeter spatial-temporal locations. For a given $1° \times 1°$ bin and a specific altimeter pass, the altimeter 1 Hz records and the model counterparts are then averaged along the ground track and form one model-altimeter collocation, provided that the total number of valid 1 Hz altimeter records is not less than 10 (see also Rascle et al., 2008). Observations from several altimeters during certain periods were excluded from our analysis for the reasons explained in Text S1.
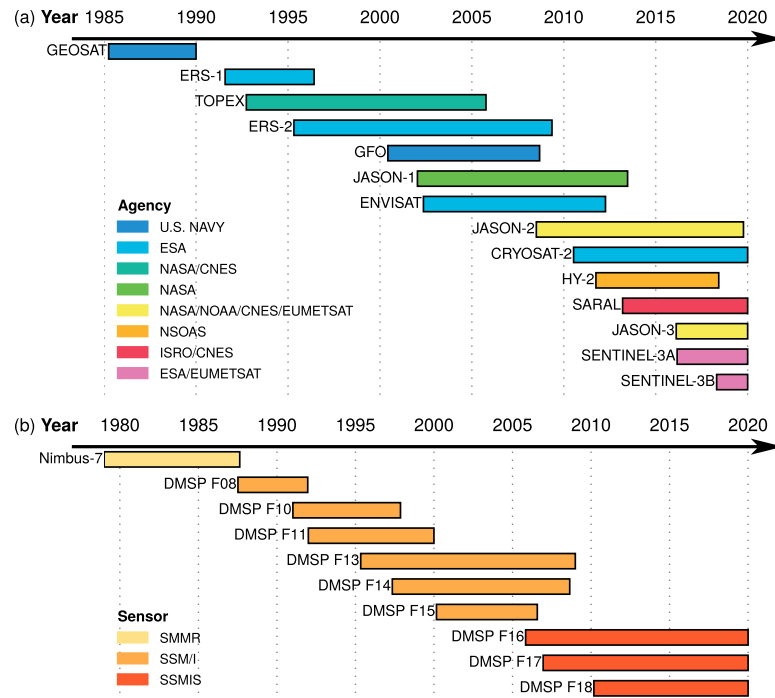
Figure 1. (a) Temporal coverage of the radar altimeter data of Ribal and Young (2019) from 14 satellite missions. Horizontal bars are color-coded according to the operating agencies. (b) Temporal extent of the passive microwave satellite data sourced from the Ocean and Sea Ice Satellite Application Facility (OSI SAF) sea ice concentration climate data records (Lavergne et al., 2019). Horizontal bars are color-coded by the type of microwave sensors.

2.2. In-Situ Wind and Wave Measurements

An extensive data set of in-situ wind and wave observations was collected as well for validating reanalysis winds and our wave hindcasts. For simplicity, hereafter we will refer to both buoys and operating platforms as "buoys." The data set consists of buoy data archived by multiple agencies, including the U.S. National Data Buoy Center (NDBC; Meindl & Hamilton, 1992), Coastal Data Information Program (CDIP; Seymour et al., 1985), Canadian Marine Environmental Data Section (MEDS), ECMWF (Bidlot, 2017; Appendix A), Chinese Ocean Monitoring Network (Wang et al., 2019), Korea Meteorological Agency (KMA), Korea Hydrographic and Oceanographic Agency (KHOA; Ha et al., 2019), Australian Ocean Data Network (AODN) and Brazilian Navy PNBOIA (Pereira et al., 2017). A few buoys located in the Southern Ocean were sourced from Ocean Observatories Initiative (Trowbridge et al., 2019) and MetOcean Solutions (see also Young et al., 2020). We have only considered buoys reporting wave data (with/without wind data). The details of each buoy data set, including the data duration, total number of stations, available wind and wave parameters, are summarized in Table 2.

Only buoys with water depth $d \geq 100$ m were chosen, except for stations in the coastal areas of China, South Korea, and Australia. Apart from the built-in quality control procedure performed by distinct agencies, we also conducted an extra statistical pre-processing to eliminate data outliers by following Caires and Sterl (2003) and Liu et al. (2016). Wind measurements U_z at non-standard height (i.e., $z \neq 10$ m) were transformed into U_{10} by assuming a neutral logarithmic boundary layer and employing the drag law of Hwang (2011). Unless otherwise specified, only U_{10}, H_s and representative wave periods (i.e., mean zero-crossing period $T_{0,2}$ or peak period T_p) were used for comparisons, and buoys with less than 1 year valid H_s records were not considered. Some buoys may change their locations many times during their lifetime because of redeployment. When collocating with model outputs (hourly spectra at buoy locations), one buoy with multiple deployments was regarded as separate stations; nonetheless, validation statistics were finally re-collected as if this specific buoy has never moved. Figure 2 presents the locations of the selected 373 buoys.

Table 2
Buoy Data Sets Considered in Our Validation

Region/Agency	Duration	#[a]	d_{min} (m)	Parameters	Source
NDBC	01/1979–12/2018	102	100	$U_z, \theta_u, H_s, T_{0,2}, T_p, \theta_w, E(f), F(f,\theta)$	NOAA Marine Environmental Buoy Database
CDIP	09/1991–10/2019	47	100	$H_s, T_{0,2}, T_p, \theta_p, E(f), F(f,\theta)$	Coastal Data Information Program
MEDS	01/1979–10/2019	28	100	$U_x, \theta_u, H_s, T_p, E(f)$	Canadian Wave Data, Fisheries and Oceans Canada
ECMWF	08/1991–03/2019	78	100	$U_z, \theta_u, H_s, T_{0,2}, T_p, \theta_w$	Coauthors J. Bidlot, G. Lemos, A. Semedo (only a subset of this data set is used; Appendix A)
COMN	01/2015–12/2016	35	0	$U_z, \theta_u, H_s, T_{0,2}, T_p, \theta_w$	Chinese Ocean Monitoring Network
South Korea	01/1996–12/2019	30	0	$U_z, \theta_u, H_s, T_x, \theta_w$	Korea Meteorological Agency; Korea Hydrographic and Oceanographic Agency
Australia	01/1979–12/2018	41	0	$H_s, T_{0,2}, T_p, \theta_p$	AODN Integrated Marine Observing System
Brazil	04/2009–12/2018	7	100	$U_{10}, \theta_u, H_s, T_p, \theta_w$	Brazilian Navy PNBOIA
Southern Ocean	04/2010–12/2019	4	100	$U_z, \theta_u, H_s, T_{0,2}, T_p, \theta_w, E(f), F(f,\theta)$	Ocean Observatories Initiative (2); Australian Ocean Data Network (1); MetOcean Solutions (1)
South Africa	01/1998–12/2003	1	100	$H_s, T_{0,2}$	Coauthor K. Machutchon

Note. Details presented include the operating agency or geographical region, duration of the entire data set, total number of buoy stations (#), minimum water depth d_{min} used to filter buoys, available wind and wave parameters (U_z, wind speed at z m above the sea surface; θ_u, wind direction; H_s, significant wave height; $T_{0,2}$, mean zero-crossing period; T_p, peak period; θ_w, mean wave direction; θ_p, peak wave direction; $E(f)$, one-dimensional wave spectrum; $F(f,\theta)$, two-dimensional wave spectrum) and corresponding data source. U_x and T_x denote that the anemometer height and the definition of the reported wave periods are undocumented.

[a]A given buoy station may correspond to multiple geographical locations due to buoy redeployment.
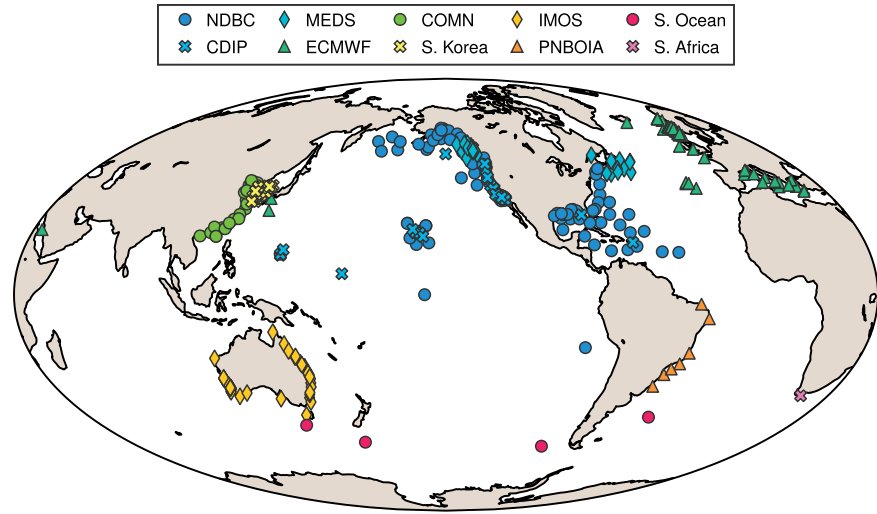
Figure 2. Locations of buoys selected to verify reanalysis winds and wave hindcasts (acronyms are introduced in Table 2).

3. Model Setup

3.1. Physics

Third generation spectral wave models solve the radiative transfer equation (RTE) to predict the evolution and propagation of ocean surface waves. Neglecting the effect of ocean currents, the RTE can be written as (e.g., Komen et al., 1994)

$$\frac{\mathrm{d}F}{\mathrm{d}t} = S_{\text{in}} + S_{\text{ds}} + S_{\text{swl}} + S_{\text{nl}} + S_{\text{bf}} + S_{\text{db}}, \tag{2}$$

where $F(f, \theta; \mathbf{x}, t)$ is the two-dimensional wave spectrum and the RHS of Equation 2 represents distinct physical processes modulating wave energy. Only physical mechanisms that are likely dominant in deep oceans, shelf seas, and shoaling zones (Young, 1999b, ch. 8) are considered here, including

1. Wind input S_{in}, wave breaking dissipation S_{ds}, and swell decay S_{swl} which are quantified by the observation-based source term package ST6 (Liu et al., 2019; Rogers et al., 2012; Zieger et al., 2015). The ST6-based wind input source function S_{in} depends on wave steepness and degree of flow separation and consequently is a nonlinear function of wave spectrum (Donelan et al., 2006). It is further subject to the physical constraint that at the sea surface, the wave-supported stress τ_w should not exceed the total wind stress $\tau = \rho_a C_d U_{10}^2$ less the viscous stress $\tau_v = \rho_a C_v U_{10}^2$ (e.g., Rogers et al., 2012; Tsagareli et al., 2010):

$$\tau_w = \rho_w g \iint \frac{S_{\text{in}}(f,\theta)}{c(f)} \Big(\cos\theta, \sin\theta\Big) \mathrm{d}f \mathrm{d}\theta \leqslant \tau - \tau_v. \tag{3}$$

here c is the phase velocity, ρ_a (ρ_w) is the density of air (water), g is the gravitational acceleration and C_d (C_v) is the total (viscous) drag coefficient. The wave breaking term S_{ds} of ST6 takes into account dissipation due to two mechanisms: (a) the inherent wave breaking occurring at each frequency once the steepness of that wave component exceeds a threshold value (Babanin et al., 2001) and (b) the induced breaking of relatively short waves due to the modulation of longer waves (Babanin, 2011; Young & Babanin, 2006). The swell decay S_{swl} parameterizes the loss of wave energy to the sea as a result of the turbulence production induced by wave orbital motions (Babanin, 2006, 2011). Swell outrunning or traveling obliquely to the wind will lose energy to the air in terms of negative S_{in} (e.g., Donelan, 1999; Liu et al., 2017). The reader is referred to Rogers et al. (2012) and Zieger et al. (2015) for full details of the ST6 package and to Liu et al. (2019) for the latest updates. Thorough comparisons of the ST6 against other source term packages can be found in Liu et al. (2019) and Stopa et al. (2016).

2. Nonlinear four-wave interactions S_{nl} as estimated by the discrete interaction approximation (DIA; Hasselmann, 1962; Hasselmann et al., 1985). Although having significant shortcomings, the DIA, being a good compromise between accuracy and efficiency, remains as the most successful parameterization of S_{nl} thus far for operational wave hindcasting and forecasting (Cavaleri et al., 2007; Liu et al., 2019; Resio & Perrie, 2008; Rogers & van Vledder, 2013; Tolman, 2013, among others).

3. Dissipation arising from the bottom friction S_{bf} (Hasselmann et al., 1973, JONSWAP). Following Zijlema et al. (2012), we have adopted the bottom-friction coefficient $\Gamma = -0.038 \, m^2 \, s^{-3}$ for both wind sea and swell.

4. Depth-induced wave breaking S_{db} due to Battjes and Janssen (1978) with the Miche-type criterion for the maximum individual wave height.

In polar regions, sea ice will damp the incident wave energy significantly in a complicated manner (e.g., Squire, 2019). While great progress has been achieved in parameterization of wave-ice interactions particularly over the past several years (e.g., Doble & Bidlot, 2013; Liu et al., 2020; Meylan et al., 2018; Rogers et al., 2016; Voermans et al., 2019; Williams et al., 2013), the ice source term S_{ice} currently available typically requires a priori knowledge of ice properties (e.g., ice thickness, rheological and/or dissipative parameters; see Table 1 of Liu et al., 2020). Yet little is known about these sea ice properties at large geophysical scales and for different ice types. For simplicity, we therefore have selected the partial-blocking approach of Tolman (2003) to represent, at least to some degree, the ice-induced wave decay. Grid cells with ice concentration $c_i > 75\%$ are regarded as land points, and with $c_i < 25\%$ as open water. For intermediate c_i, the wave energy flux is partially blocked with the amount of blocked varying linearly between 0 and 1.

3.2. Numerics

The spectral grid is discretized as $\Delta f \, / \, f = 0.1$ and $\Delta\theta = 10°$ with $f_i \in [0.037, 0.953]$ Hz, $i = 1,\dots,35$. Wave energy is propagated in the spatial and spectral spaces using the third-order ULTIMATE QUICKEST scheme with the averaging method to alleviate the Garden Sprinkler Effect (Tolman, 2002).

The global wave simulations are performed on an IRI grid system designed by Rogers and Linzell (2018, IRI-1/4 therein). Specifically, this IRI system consists of three separate grids (Figure 3), including

- a regular spherical grid at low latitudes (latitude $| \phi |\lesssim 55°$) with the spatial resolution at 0.25° by 0.25°;
- two curvilinear polar stereographic grids (Rogers & Campbell, 2009) at high latitudes (approximately $| \phi |\gtrsim 50°$) with the resolution at about 18 km.

The IRI grid technique is devised to improve model efficiency particularly for global wave simulations covering very high latitudes. This is achieved by minimizing the variability of grid spacing (Δx) which consequently allows for a larger time step as prescribed by the CFL criteria. At the overlapped zone (i.e., $\phi \in [50°, 55°]$), Δx for the regular and curvilinear grids is matched approximately at 16 km (Figure 3c). Latitudes beyond 89°N are excluded from the computations (Figure 3a) to avoid the polar singularity (Li, 2012; Rogers & Campbell, 2009). All the three grids share the same time steps with the global time step Δt_g and time steps for spatial advection Δt_x, intraspectral propagation Δt_f and source term integration Δt_s of 1800, 600, 600, and 180 s, respectively. Unresolved islands are represented as obstruction grids by following Chawla and Tolman (2008) and Tolman (2003). One is referred to Rogers and Linzell (2018) for more technical details on the IRI grid systems (e.g., configurations at four distinct resolutions, time stepping and validation). Three-hourly field outputs from these three grids are gathered and regridded onto a regular spherical global 0.25° × 0.25° grid.

3.3. Forcing Data

3.3.1. Ice Concentration

The Arctic and Antarctic sea ice concentration data, used as WW3 input, are sourced from the second version of the global c_i climate data records released by the EUMETSAT Ocean and Sea Ice Satellite Application Facility (OSI SAF; Lavergne et al., 2019, Table 1). This data set was derived from passive microwave
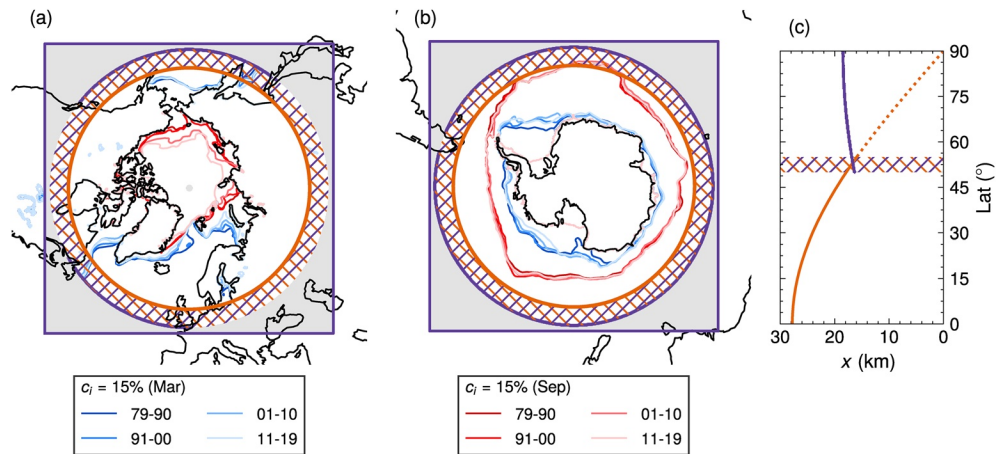
Figure 3. Illustration of the irregular-regular-irregular (IRI)-1/4 grid system at the (a) Northern and (b) Southern Hemispheres. The orange circle (latitude $\phi = 55°$) highlights the boundary of the regular spherical grid at low latitudes. The purple rectangle defines the spatial extent of the curvilinear polar stereographic grid, where the gray-shaded region is masked out in WAVEWATCH III simulations and the purple circular arcs along $\phi = 50°$ denote active boundary points. The climatological sea ice edges (ice concentration $c_i = 15\%$) in March and September for each decade are also shown as blue and red contour lines. (c) Evolution of the grid spacing Δx (in km) with latitude ϕ for the (solid orange) regular and (purple) curvilinear grids (figure adapted from Figure 8 of Rogers & Linzell, 2018). The dotted orange line indicates how Δx of the regular grid changes if ϕ further increases. The hatched region in each panel represents the overlapped zone between different grids.

satellite records provided by the Scanning Multichannel Microwave Radiometer (SMMR), Special Sensor Microwave/Imager (SSM/I), and Special Sensor Microwave Imager/Sounder (SSMIS) instruments onboard the U.S. Defense Meteorological Satellite Program (DMSP) satellites (Figure 1b). A hybrid, self-tuning and self-optimizing algorithm was employed to retrieve c_i from brightness temperature using imaging frequency channels at 19 and 37 GHz (Lavergne et al., 2019). The processed daily c_i data are delivered on two Equal Area Scalable Earth 2 (EASE2) grids at the resolution of 25×25 km^2. When forcing WW3, significant data gaps of this OSI SAF data set (e.g., 03/1986–06/1986) were filled by the ERA5 c_i product.

3.3.2. Wind Forcing

Wind forcing stands as one critical component for spectral wave modeling. Various reanalyzed wind data sets are available, among which the two modern reanalyses have been considered in this study (Table 1), namely the ERA5 global reanalysis ($0.25° \times 0.25°$; Hersbach et al., 2020) and the CFS reanalysis ($0.5° \times 0.5°$; Saha et al., 2010; Saha et al., 2014, sourced from https://rda.ucar.edu). A detailed intercomparison of the ERA5 and CFS winds against the altimeter U_{10} is first conducted to understand their relative performance on the global scale. Bidlot et al. (2019) demonstrated that wave simulations forced by the ERA5 10 m neutral winds $U_{10,neu}$ slightly outperform those forced by the ERA5 conventional U_{10}, as characterized by the reduced positive (negative) bias in H_s under stable (unstable) atmospheric stratification (see also Cordero et al., 2020). We therefore included the ERA5 $U_{10,neu}$ in the intercomparison analysis as well. It is noteworthy that altimeter U_{10} was not assimilated into the ERA5 and CFS forecasting systems (Hersbach et al., 2020; Saha et al., 2010, 2014), and thus is fully independent from these reanalyzes. Error metrics used below include bias b, root mean square error ($RMSE$) ϵ, correlation coefficient ρ, scatter index (SI) and normalized bias b_n and $RMSE$ ϵ_n, of which definitions can be found in Ardhuin et al. (2010) and Chawla et al. (2013), among others, and therefore are not described here.

Figure 4 presents the comparison of winds between altimeters (ENVISAT, JASON-1/2 and CRYOSAT-2) and different reanalyses for the year 2011. It is seen that the ERA5 U_{10} and $U_{10,neu}$ are in remarkable agreement with altimeter measurements (Figures 4a and 4b), showing a correlation (ρ) of 0.95 and scatter index (SI) of 0.14. Both of the ERA5 winds underestimate altimeter values slightly with biases (b) of -0.41 and -0.25 m s^{-1} for the conventional and neutral U_{10}, respectively. In terms of the $RMSE$ (ϵ), the ERA5 $U_{10,neu}$ is
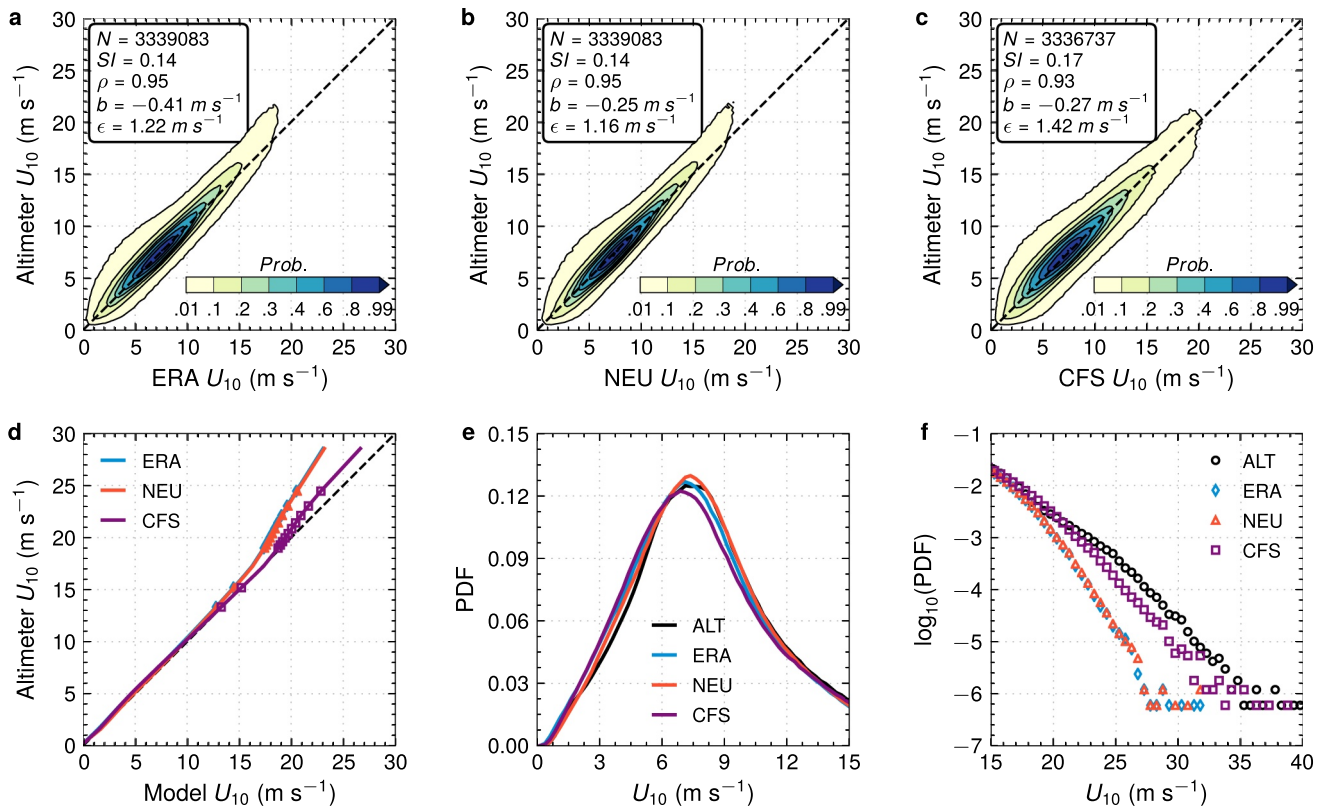
Figure 4. Comparison of winds between altimeters (ENVISAT, JASON-1/2, CRYOSAT-2) and reanalyzes (a) ERA5 U_{10}, (b) ERA5 neutral winds $U_{10,neu}$, and (c) NCEP climate forecast system (CFS) U_{10} for 2011. (d) The percentile plot (i.e., Q-Q plot) of U_{10} with markers highlighting the 90, 95, 99, 99.1, …, 99.9th percentiles. (e) Estimated probability density functions (PDFs) of U_{10} for $U_{10} \leq 15$ m s^{-1}. (f) Same as (e) but for PDFs plotted on a logarithmic scale and for higher winds ($U_{10} > 15$ m s^{-1}). "NEU" in (d)–(f) represents the ERA5 neutral winds $U_{10,neu}$.

marginally better than the conventional U_{10} (1.16 vs. 1.22 m s^{-1}). The CFS U_{10} also compares well with altimeters (Figure 4c), but yields noticeably weaker skills than the ERA5-based ones, as illustrated by the relatively higher ϵ and SI (1.42 m s^{-1}, 0.17) and lower ρ (0.93). On average, U_{10} from the CFS is 0.27 m s^{-1} lower than observations. It may be worth mentioning that the differences in the performance of the ERA5 and CFS winds could not be explained by the relatively coarse resolution of the CFS data we selected (i.e., 0.5°). The CFS U_{10} archived on the native T574 reduced Gaussian grid (~ 0.2°) presents very similar error metrics to those given in Figure 4c (see e.g., Figure 2 of Stopa et al., 2016). The percentile-percentile or QQ plot (Figure 4d) suggests that all the three reanalysis winds perform well up to the 95th percentile of occurrence. For even higher wind speeds (e.g., 99–99.9th percentiles or $U_{10} > 20$ m s^{-1}), the ERA5 clearly underestimates the altimeter retrievals based on Equation 1. The CFS, on the other hand, shows a better performance in representing these extreme conditions, as distinctly evidenced by the estimated PDFs (Figure 4f).

The spatial distributions of the normalized bias b_n and $RMSE$ ϵ_n of the three reanalysis winds in 2011 are shown in Figure 5. Both ERA5 and CFS U_{10} show negative biases (~-6% and −3%, respectively) dominating over the global basins except for the area off the Pacific coast of northern South America (Figures 5a and 5e). This corresponds well to the Niño 3 region defined by the climate community (Rasmusson & Carpenter, 1982), and U_{10} is moderately overestimated particularly for the CFS. At high latitudes (e.g., Southern Ocean), the ERA5 U_{10} is significantly lower than altimeter observations ($b_n \sim -9\%$), whereas the CFS winds are markedly stronger and have a $b_n \sim -3\%$. On the contrary, in the equatorial zones (e.g., the Intertropical Convergence Zone; ITCZ), the CFS U_{10} is more negatively biased than the ERA5 (−15% vs. −9%).

The regional variation in the ϵ_n of the ERA5 U_{10} (Figure 5b) is quite remarkable. The lowest ϵ_n is seen in the central eastern Pacific and Atlantic Oceans (7%), followed by 10% in the Southern Ocean. Errors in the western Pacific and Atlantic are markedly larger (15%–20%), and the largest errors appear in the equatorial
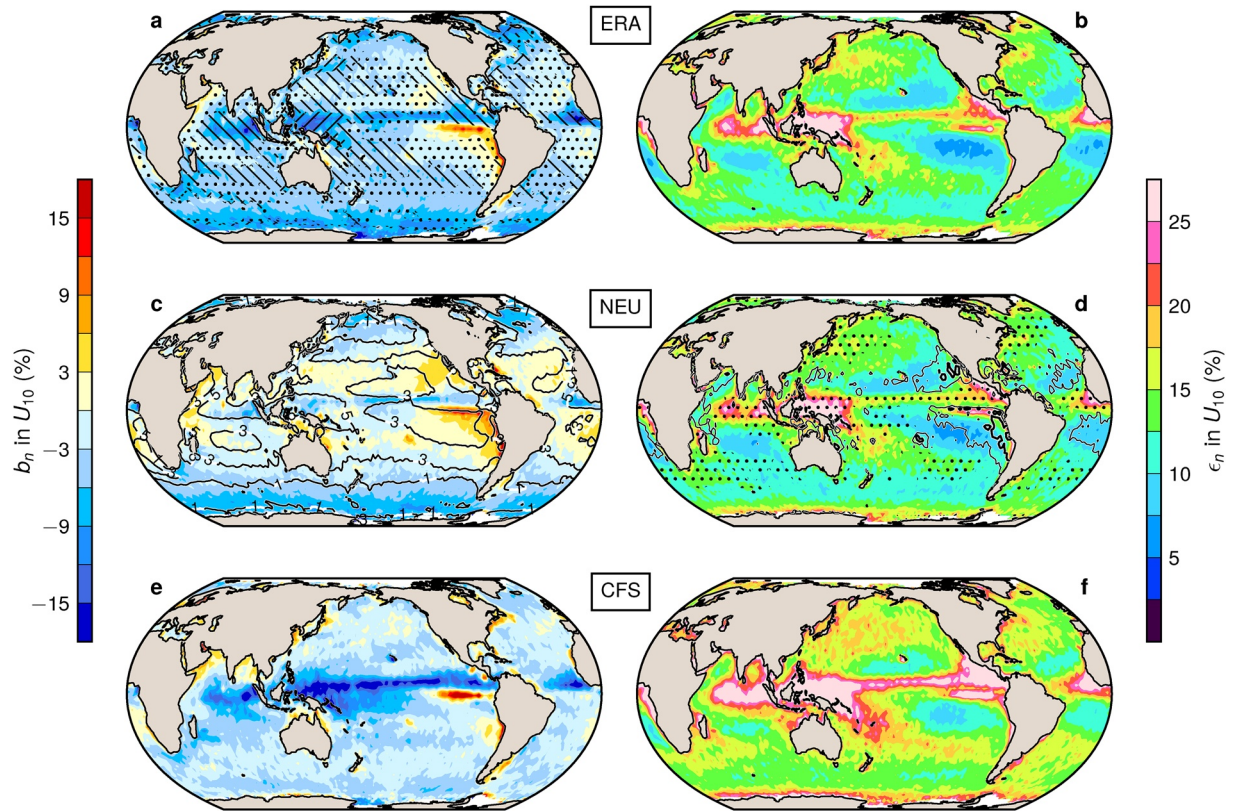
Figure 5. Error metrics of winds gridded in 2° × 2° bins for (a and b) ERA5 U_{10}, (c and d) ERA5 neutral winds $U_{10,\text{neu}}$, and (e and f) NCEP climate forecast system (CFS) U_{10} in 2011, showing (left) normalized bias b_n and (right) normalized rmse ϵ_n. Hatching in (a) represents the contour level of $\Delta T_n = (T_2 - T_s) / T_2$, with '/', '\' and '.' corresponding to $\Delta T_n < -7, -5, -3‰$, respectively. Here T_2 and T_s are the annual mean air temperature at a height of 2 m and sea surface temperature. Contours in (c) denote the relative difference in b_n between the ERA5 conventional and neutral winds, $\Delta b_n = b_{n,U_{10,\text{neu}}} - b_{n,U_{10}}$. Stippling in (d) indicates where $\Delta \epsilon_n = \epsilon_{n,U_{10,\text{neu}}} - \epsilon_{n,U_{10}} < -1\%$, and black thin and thick contours are for $\Delta \epsilon_n$ of 0% and 1%, respectively.

zones, especially in the vicinity of the Maritime Continent (> 25%). Chelton and Xie (2010) pointed out that present-day numerical weather prediction models tend to underrepresent the mesoscale influence of sea surface temperature (SST) on surface winds, explaining well the relatively larger errors in winds riding on the western boundary currents (e.g., Kuroshio and Gulf Stream). Besides, the Gulf Stream and the Kuroshio Current regions are also areas where intense cyclogenesis activity is taking place, which is not always well captured by atmospheric models. The CFS U_{10} provides a very similar error pattern (Figure 5f) but the ϵ_n is generally 3%–5% higher in central basins than that for the ERA5.

Also shown in Figure 5a is the relative difference between the annual mean 2 m air temperature T_2 and SST T_s, defined by $\Delta T_n = (T_2 - T_s) / T_2$ (the hatching). Consistent with Young and Donelan (2018), the vast majority of the global oceans are characterized by unstable atmospheric stratification (i.e., negative ΔT_n). According to the Monin-Obukhov similarity theory (Monin & Obukhov, 1954), the equivalent neutral winds $U_{10,\text{neu}}$, transformed from U_{10}, will be stronger than U_{10} (see e.g., Figure 2 of Young & Donelan, 2018). Figure 5c demonstrates clearly that in most regions the ERA5 $U_{10,\text{neu}}$ is 3%–5% higher than the conventional U_{10} (black contours). In low and mid latitudes, the $U_{10,\text{neu}}$ slightly overestimates altimeter values ($b_n \sim 3\%$). The relative performance of the ERA5 $U_{10,\text{neu}}$ over the conventional U_{10} is not spatially uniform (Figure 5d). On the west side of ocean basins, ϵ_n for the $U_{10,\text{neu}}$ is 1% lower (stippling); by contrast, ϵ_n in the eastern ocean basins is enlarged marginally (~ 1%; black contours). It should be noted, however, that the altimeter U_{10} effectively assumes neutral conditions as they were calibrated against buoy observations (U_z) extrapolated to 10 m under a neutral boundary layer assumption (Young & Donelan, 2018). Therefore, it is not surprising that overall, the ERA5 $U_{10,\text{neu}}$ is marginally closer, than the conventional U_{10}, to the altimeter data (Figures 4a and 4b).
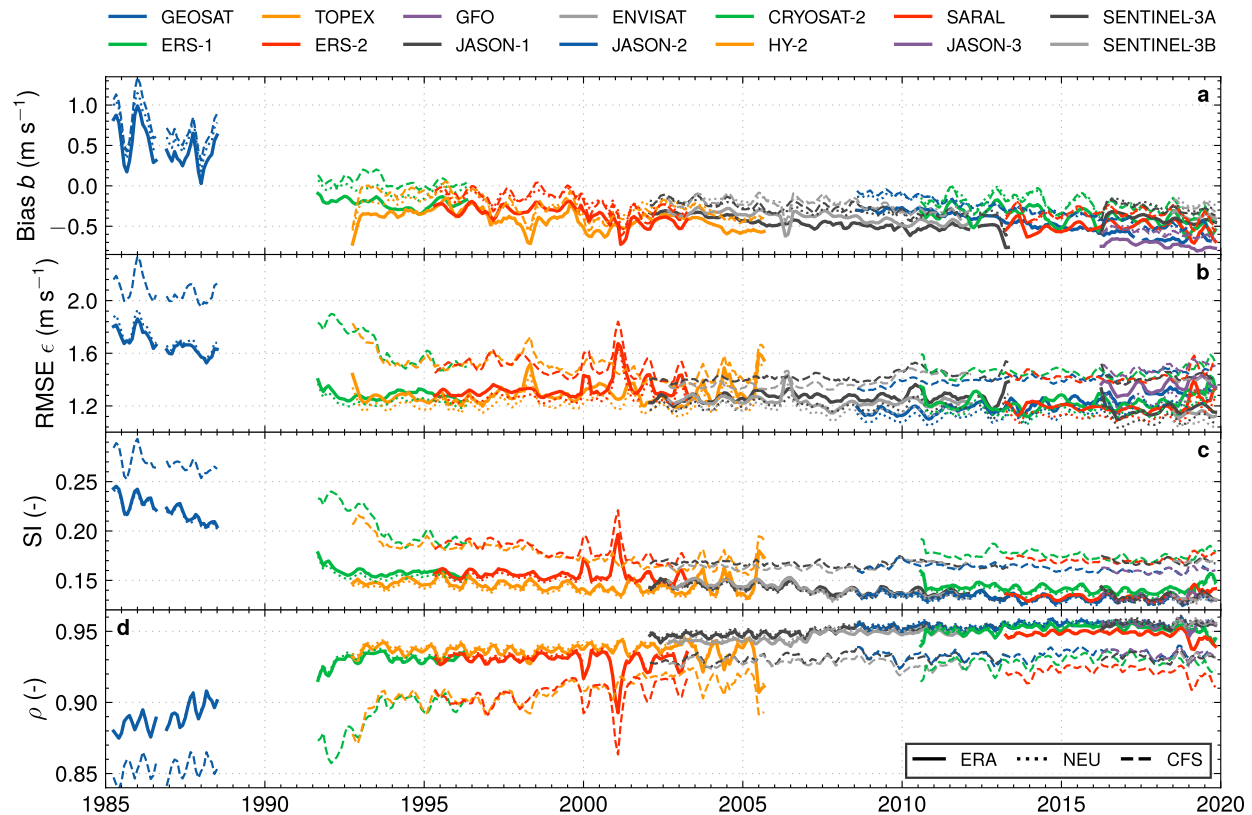
Figure 6. Evolution of error metrics with time of three reanalysis winds (solid lines: ERA5 U_{10}, dotted lines: ERA5 neutral winds $U_{10,neu}$, dashed lines: NCEP climate forecast system (CFS) U_{10}) relative to different altimeters: (a) bias b, (b) RMSE ϵ, (c) scatter index (SI), and (d) correlation coefficient ρ. Following Chawla et al. (2013), monthly statistics are calculated for a sliding 3 month period for the global domain. The ERS-2 was operated without gyroscopes after February 2001, and thus data quality has degraded slightly since then, as clearly illustrated by the jump occurring in 2001.

Figure 6 presents the temporal evolution of error metrics of the three reanalysis winds relative to all the altimeters for the global domain. Following Chawla et al. (2013), monthly statistics are calculated over a sliding 3 month period. It is demonstrated that the systematic differences across distinct winds are fairly consistent over time. In line with Figure 4, the RMSE of the ERA5 $U_{10,neu}$ is generally the lowest, very closely followed by the ERA5 U_{10}, whereas the CFS U_{10} yields noticeably larger ϵ (Figure 6b). During the early period of the altimeter epoch (e.g., GEOSAT and ERS-1 missions prior to 1993), the mismatch between reanalyses and satellite observations is remarkably large. Subsequently, skills of the ERA5 and CFS winds are appreciably improved, showing a clear, continuous reduction (increase) in SI (ρ) over the years (Figures 6c and 6d). This is primarily due to the growing availability of observations for data assimilation (see e.g., Figure 3 of Hersbach et al., 2020). Error metrics from 2010 onwards, particularly after 2015, become more or less stable. The performance of the upper percentile reanalysis winds (i.e., 90th-, 95th- and 99th-percentiles) is further discussed in Appendix B.

Considering that (a) the ERA5 winds are significantly of better quality than the CFS winds, as characterized by the noticeably lower random errors (SI) and relatively better homogeneity in time, and (b) that the differences in the ERA5 conventional and neutral winds are marginal, we therefore have chosen the ERA5 conventional U_{10} as the wind forcing for our long-term global wave hincast from 1979 to 2019. Nonetheless, the CFS winds perform extremely well at high winds (e.g., $U_{10} > 20$ m s^{-1}) particularly after the year 2010 (Figures B1a, B1c and B1e). Hence, we also performed a short-term nine-year model run (from 2011 onwards) with the CFS U_{10}. Similarly, another nine-year run with the ERA5 neutral winds was also conducted, aiming at understanding the response of the ST6 wave physics to the atmospheric stability.

Table 3
Summary of the WW3-ST6 Global Wave Hindcasts With Different Wind Forcings

Wind Forcing	CDFAC	Period
ERA5 U_{10}	1.08	1979–2019
ERA5 $U_{10,neu}$	1.06	2011–2019
CFS U_{10}	0.98	2011–2019

Note. Here CDFAC represents the tunable wind stress parameter of the ST6 package (Zieger et al., 2015).

The ST6 source term package available in WW3 (version 6.07 and higher) was initially calibrated with one-year of CFS data for 2011 (Liu et al., 2019). It provokes a re-calibration of the tunable wind stress parameter, CDFAC, of the ST6 when different winds are adopted (Zieger et al., 2015), defined by

$$u_*^2 = \textbf{CDFAC} \cdot C_d U_{10}^2, \tag{4}$$

where u_* is the wind friction velocity. In this study, we used CDFAC of 0.98, 1.06, and 1.08 for the CFS U_{10}, ERA5 $U_{10,neu}$ and conventional U_{10}, respectively (Table 3). The CFS-based run corresponds to the lowest CD-FAC owing to the fact that the CFS is the strongest among the three winds selected, especially for extreme winds (Figure 4, Figure B1). Once again, these values were calibrated based on a single-year model run for 2011 (see next section), and then applied throughout the entire simulation period.

4. Validation Against Satellite Altimeter Observations

The global wave hindcasts forced by three different winds for the year 2011 are inter-compared against altimeter H_s observations (ENVISAT, JASON-1/2, CRYOSAT-2, and HY-2) in Figure 7. It is observed that, once calibrated (through CDFAC), the ERA5-based simulations are in excellent agreement with satellite observations (Figures 7a and 7b). The simulated H_s is almost unbiased ($b = 1$ cm) and the RMSE ϵ is about 0.3 m. Meanwhile, the scatter index (*SI*) is low (0.12) and the correlation coefficient (ρ) is as high as 0.97. Consistent with Bidlot et al. (2019), H_s in the run forced by the ERA5 $U_{10,neu}$ is marginally better predicted ($\epsilon = 0.31$ vs. 0.33 m). The CFS-based H_s is very promising as well (Figure 7c), but again, presents slightly weaker scores ($\epsilon = 0.39$ m, $\rho = 0.96$, $SI = 0.14$). This is not surprising since the quality of the surface wind field is a crucial factor determining the accuracy of wave simulations (Janssen, 2008). The QQ plot further demonstrates that both the ERA5- and CFS-based simulations perform well at upper percentiles (below 99th-percentile; Figure 7d). When extreme sea states are considered (e.g., $H_s > 8$ m), H_s from the CFS run matches the observed PDF much better (see also Rascle & Ardhuin, 2013); whereas simulations with the ERA5 winds clearly underestimate the most extreme seas ($H_s > 14$ m) due to the under-specified high winds (Figures 7f and 4f).

Figure 8 illustrates the spatial distribution of the H_s errors based on the three different winds for 2011. The normalized bias, yielded by the ERA5 and CFS U_{10} (Figures 8a and 8e), presents a typical global error pattern given by the ST6 physics (Liu et al., 2019; Zieger et al., 2015): negative (positive) bias in the western (eastern) Pacific Ocean, and the overall overestimation in the entire Southern Ocean. In general, the run with the ERA5 U_{10} overestimates H_s by about 4% in the eastern Pacific Ocean, southern Atlantic Ocean, western Indian Ocean and the Southern Ocean. By contrast, H_s in the remaining regions is underestimated by 4%–8% (Figure 8a). The CFS-based H_s on average is more biased: wave heights in the Southern Ocean are over-predicted by around 8%, and in the western tropical Pacific Ocean are under-specified by 12% or more (Figure 8e). Unlike the run with the ERA5 U_{10}, negative biases of H_s (4%–8%) dominate over the central Atlantic and Indian Oceans in the CFS run. The normalized *RMSE* of the simulated H_s has considerable spatial similarities with that for the driving wind forcing. It is evident from Figures 8b and 8f that model runs with the ERA5 and CFS U_{10} present higher ϵ_n in the western Pacific and Atlantic Oceans than in the central eastern part of these basins. Our simulations did not consider wave-current interactions, which could also be a factor for larger errors along the path of western boundary currents (such as Gulf Stream off the U.S. east coast). The maximal ϵ_n is observed in the proximity of the Maritime Continent and the Antarctic. Spe-
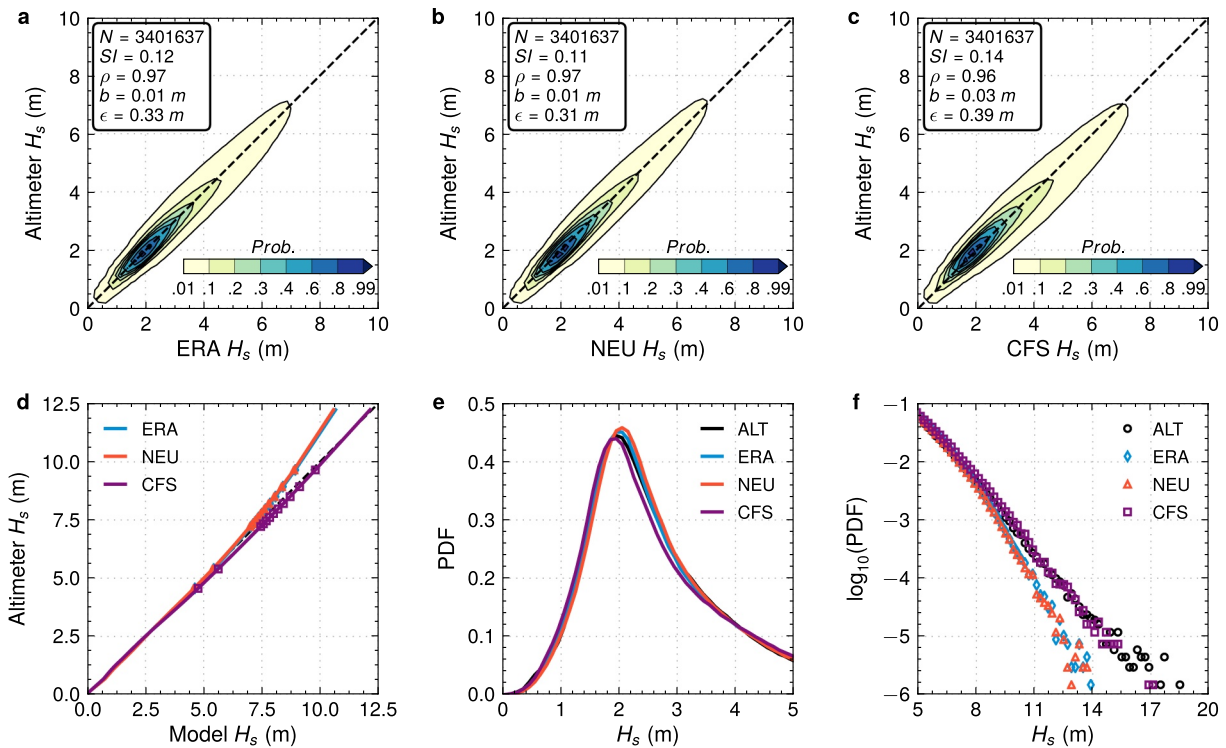
Figure 7. Comparisons of H_s between altimeters (ENVISAT, JASON-1/2, CRYOSAT-2, and HY-2) and WW3-ST6 hindcasts forced by the (a) ERA5 U_{10}, (b) ERA5 neutral winds $U_{10,neu}$ and (c) NCEP climate forecast system (CFS) U_{10} in 2011. (d) The percentile plot (i.e., Q-Q plot) of H_s with markers highlighting the 90, 95, 99, 99.1, …, 99.9th percentiles. (e) Estimated probability density functions (PDFs) of H_s for $H_s \leq 5$ m. (f) Same as (e) but for PDFs plotted on a logarithmic scale and for higher sea states ($H_s > 5$ m).

cifically, the run forced with the ERA5 U_{10} corresponds to $\epsilon_n \sim 10\%$ in the central Pacific Ocean and in the Southern Ocean, ϵ_n about 14% in the northwest Pacific and Atlantic, and ϵ_n around 20% in the equatorial zone of the west Pacific (Figure 8b). The CFS-based ϵ_n is generally 2% higher in most regions (Figure 8f). Further discussions about the spatial distribution of wave model errors can be found in Liu et al. (2019, their section 5.a) and Ardhuin et al. (2010).

As expected, the hindcast forced by the ERA5 neutral winds does not deviate significantly from the run with the ERA5 conventional U_{10} (Figure 8c). Changes in both wind speed and CDFAC (Figure 5c and Table 3), working together, give rise to slightly higher H_s (1%–3%) in the low and mid latitudes, but lower H_s (1%) in the high latitudes (black contours in Figure 8c). The ϵ_n is reduced by 1% in the western tropical Pacific, Southern Ocean and in the regions close to Kuroshio and Gulf Stream (stippling in Figure 8d). By contrast, the ϵ_n increases to a small degree (about 1%) in the central eastern Pacific and western Indian Ocean (black contours in Figure 8d).

Figure 9 displays the monthly error metrics of the simulated global H_s during the satellite era 1985–2019. Once again, there is an apparent improvement in the ERA5-based model skills (ϵ, SI, and ρ; solid lines in Figures 9b–9d) over the past decades as a result of enhanced wind data (Figure 6). The SI changes from 0.13 to 0.14 for the GEOSAT to 0.11–0.12 for the latest altimeters (e.g., JASON-3 and SENTINEL-3A/B). The biases show a fairly complex pattern, ranging from −15 cm for the ERS-1/2 and TOPEX satellites to 5 cm for altimeters operating after 2010 (Figure 9a). At first sight, this would seem to imply that the model bias is clearly inhomogeneous in time. A close inspection of Figure 9a, however, suggests that the change in the sign of model biases (from negative to positive) taking place around 2010 is primarily attributed to the systematic differences in H_s across distinct altimeters. It is seen that H_s from ENVISAT and JASON-1 on average is 8 cm higher than that from the concurrently operating JASON-2 altimeter (see also Figure 7 of Ribal & Young, 2019). Similarly, a systematic difference of 5 cm in H_s exists between the TOPEX and JASON-1 altimeters during 2003–2005. The spike in TOPEX occurring in 1997 and 1998 is known as the
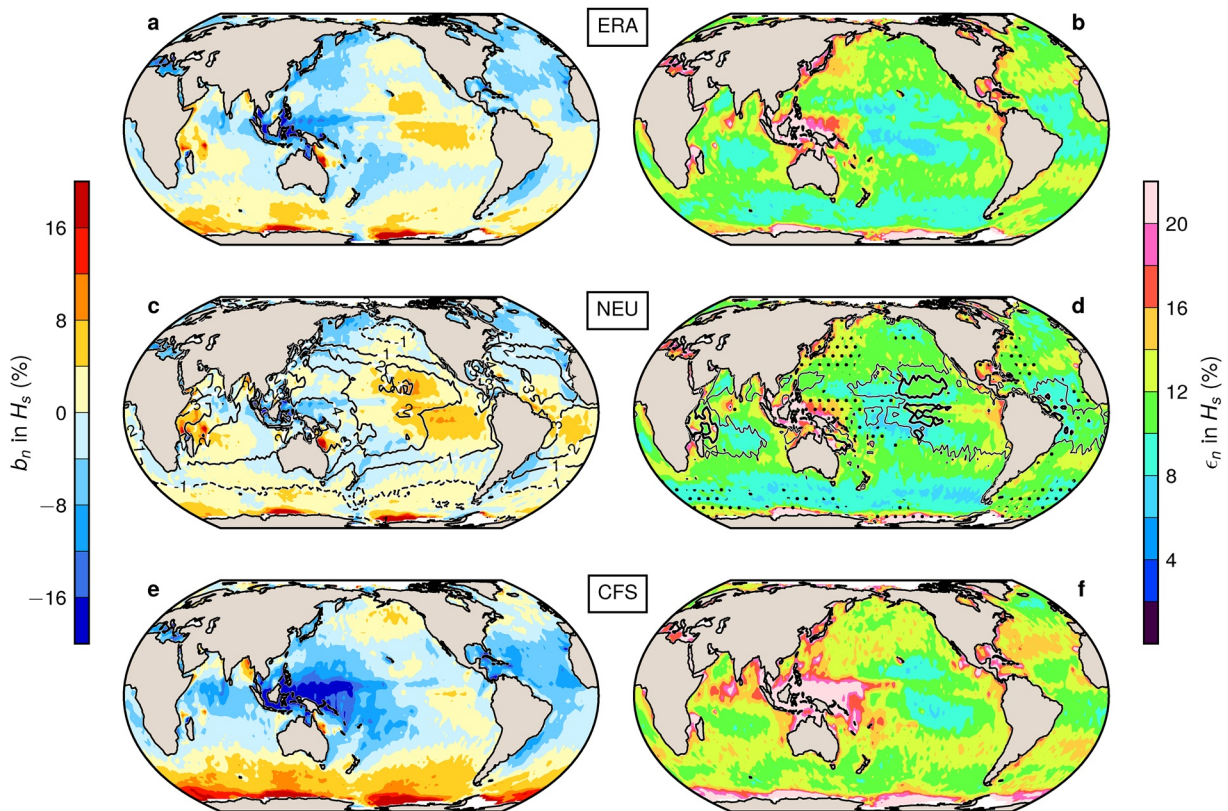
Figure 8. Error metrics of H_s gridded in $2° \times 2°$ bins according to WW3-ST6 forced by the (a and b) ERA5 U_{10}, (c and d) ERA5 neutral winds $U_{10,\mathrm{neu}}$, and (e and f) CFS U_{10} in 2011. Contours in (c) denote $\Delta b_n = b_{n,\mathrm{NEU}} - b_{n,\mathrm{ERA}}$. Stippling in (d) indicates where $\Delta \epsilon_n = \epsilon_{n,\mathrm{NEU}} - \epsilon_{n,\mathrm{ERA}} < -1\%$, and black thin and thick contours are for $\Delta \epsilon_n$ of 0% and 1%, respectively.

TOPEX drift (e.g., Zieger et al., 2009). Although having been largely removed during calibration, a residual of the drift is still appreciable.

Figure 10 further supports the previous argument about systematic biases among altimeters. When compared against another independently calibrated altimeter data set, that is, the Sea State Climate Change Initiative (CCI) data set (L4 product; Dodet et al., 2020), from which the calibrated H_s of the ENVISAT, JASON-1 and JASON-2 is more consistent (particularly during 2006–2012; see their Figure 11), our model bias is more uniformly distributed over time (red line in Figure 10), showing a underestimation by about 5 cm except for the period prior to 1995. It should be stressed, however, that these inter-comparisons do not necessarily indicate that one altimeter data set outperforms another. Instead, it highlights the possible inconsistency in the altimeter H_s arising from different calibration methodology. Ribal and Young (2019) used in-situ NDBC buoy observations as the "ground truth", whereas the CCI data, particularly for H_s from the most recent missions (i.e., JASON-1/3, CRYOSAT-2, and SARAL), were corrected against their JASON-2 data (which is, on average, positively biased, in 8 cm, in comparison with buoy records; see Figure 10 of Dodet et al., 2020). As will be seen later, the evolution of model biases relative to altimeters from Ribal and Young (2019) is actually well-supported by that for in-situ NDBC buoys (Figure 12b). These discrepancies, as a whole, imply possible inhomogeneities existing in the NDBC wave measurements, which are not unexpected due to changes in buoy hulls and data processing algorithms over time (Gemmrich et al., 2011). In this regard, Ardhuin et al. (2019, their section 3.2) mentioned that "*before 2009, the vast majority of wave buoys in North America were based on strapped-down accelerometers. Since then, NOAA-NDBC modified their on-board packages correcting the error, but a large number of historical buoy records have not been corrected*". Ardhuin et al. (2019) further showed that H_s from the strapped-down accelerometer is generally higher than values from the modern, HIPPY™ sensor, particularly for H_s above 6 m (their Figure 6). This fact seems highly relevant for the discrepancies we just discussed. It is therefore recommended to adopt
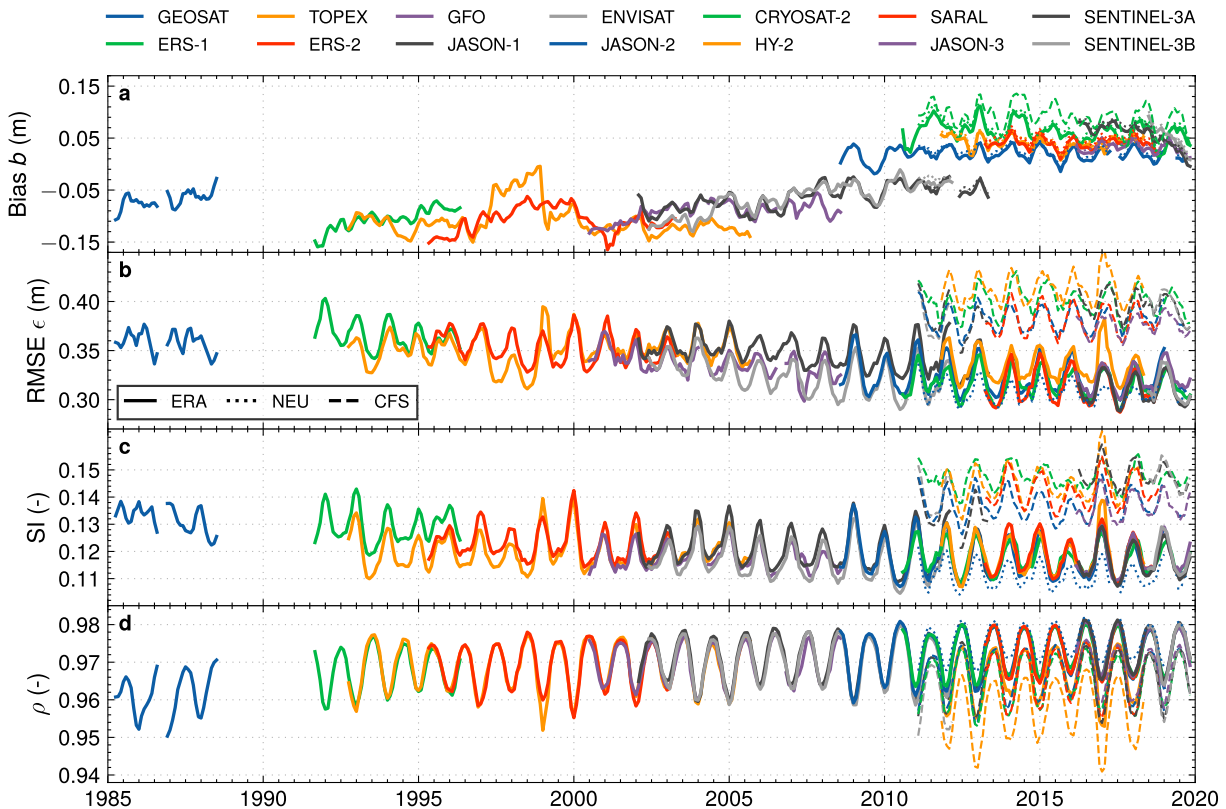
Figure 9. Same as Figure 6 but for the error metrics of H_s for the global domain. The solid, dotted and dashed lines represent the WAVEWATCH III (WW3)-ST6 hindcasts forced by the ERA U_{10}, ERA neutral $U_{10,neu}$ and NCEP climate forecast system (CFS) U_{10}, respectively. For clarity, only the bias b from CRYOSAT-2 is shown for the CFS-based ST6 hindcast in panel (a); similarly, only metrics from JASON-2 are shown in panels (b)–(d) for the ERA5 $U_{10,neu}$-based run.

high-quality wave hindcasts as a complementary reference for future calibration and validation of altimeter wave records (e.g., Caires & Sterl, 2003; Liu et al., 2016).

The hindcast with the CFS winds (dashed line in Figure 9) provides slightly higher random errors and lower correlation coefficients. Consistent with Figure 7, the run with the ERA5 neutral winds (dotted line in Figure 9) is marginally better than that driven by the ERA5 conventional winds. The seasonal variability of the SI is also noticeably reduced in the ERA5 $U_{10,neu}$-based run (Figure 9c). The upper percentile simulated wave height is further analyzed in Figures B1b, B1d and B1f and Appendix B.

5. Validation Against In-Situ Measurements

5.1. Conventional Parameters

The entire 41-years ST6 wave hindcast, forced by the ERA5 conventional U_{10}, is compared against all the buoy observations available in Figure 11. Only wave height H_s and mean wave period $T_{0,2}$ are presented and the data duration from each buoy can be found in Figure S1. On the whole, the hindcast presents a negative bias generally within 10 cm (5%) for H_s, particularly in deep oceans. This corresponds to a SI less than 0.15 (Figure 11b). A few buoys in the Southern Ocean show positive biases within 10–20 cm (<5%), fairly consistent with the errors found from altimeter data (Figure 8a). Errors in H_s clearly increase when moving closer to the coast. The random error (SI) near the U.S. east and west coasts is roughly 0.15–0.2, and even higher in the Australian east coast (0.2–0.3) and in the East China and Yellow seas (>0.4). This is not surprising since most of the
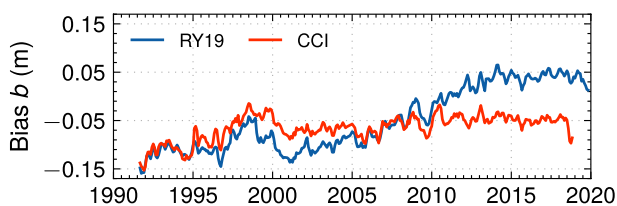

Figure 10. The monthly bias of H_s in the ST6 global hindcast forced by the ERA5 U_{10} relative to different merged altimeter data sets: (blue) the data set of Ribal and Young (2019), (red) the Sea State Climate Change Initiative (CCI) data set (L4 product; Dodet et al., 2020).
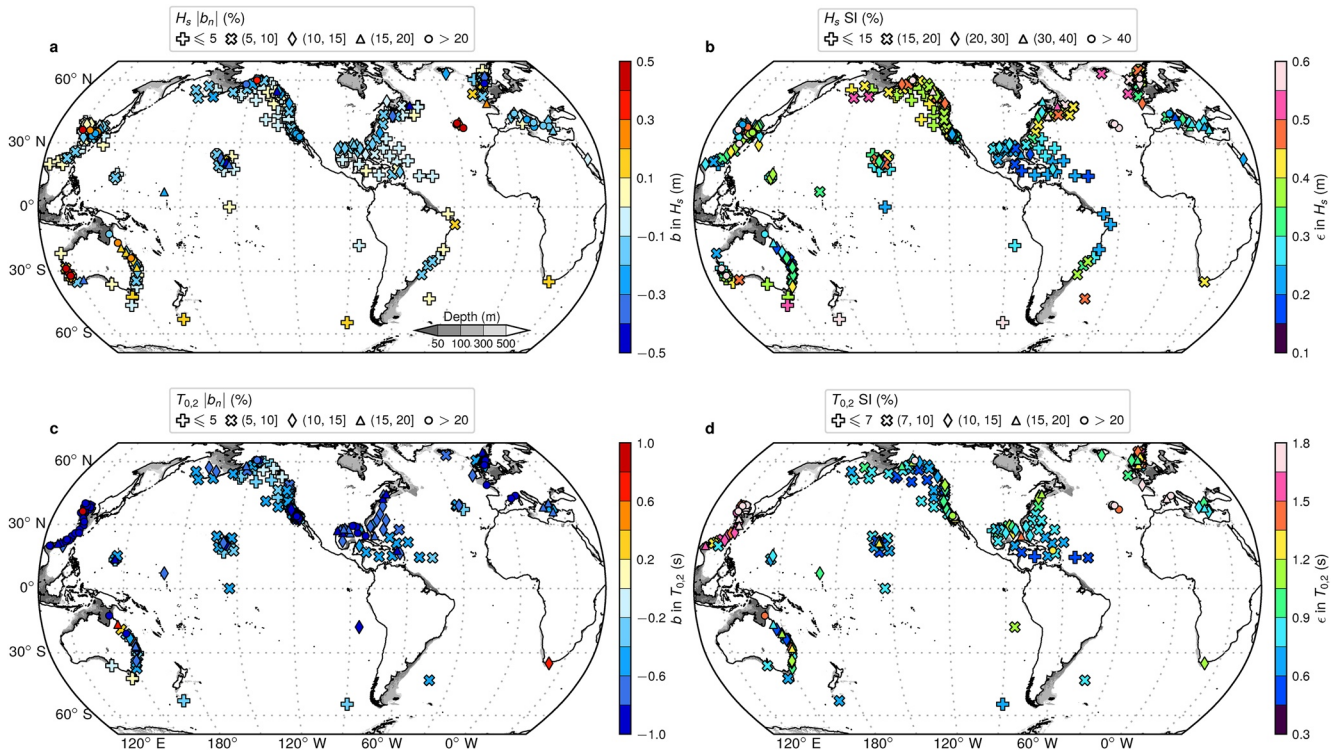
Figure 11. Comparison of the 41-years ST6 wave hindcast against in-situ buoy measurements. Colors and symbols in each panel represent: (a) bias b of H_s (in m) and normalized bias $|b_n|$ (in %), (b) *RMSE* ϵ of H_s (in m) and *SI* of H_s (in %), (c) bias b of the mean wave period $T_{0,2}$ (in s) and normalized bias $|b_n|$ (in %), and (d) ϵ of $T_{0,2}$ (in s) and the corresponding *SI* (in %). The gray shaded contour highlights regions shallower than 500 m.

Australian, Chinese, and Korean buoys are located in rather shallow waters ($d \leq 100$ m; see also Table 2). Wave heights in the Gulf of Mexico and Mediterranean sea are noticeably underestimated (about 10%–20%), and show a random error larger than 0.2. Considerable errors in these marginal seas and semi-enclosed basins suggested that the 0.25° model configuration is not sufficient to resolve complex coastlines and bathymetry varying on smaller spatial scales. The effect of currents and tides on the wave field may also become pronounced in these coastal regions (e.g., Ardhuin et al., 2012; Rapizo et al., 2017). In this respect, high-resolution wave hindcasts around the Australian coast and in the China seas, using refined unstructured grids (Abdolali et al., 2020; Roland, 2008), will be performed in the future.

The mean wave period $T_{0,2}$ is globally underestimated by around 0.6 s (less than 10%) in the open waters (Figure 11c), corresponding to a *SI* below 0.1 (Figure 11d). Note that the modeled $T_{0,2}$ was estimated from the simulated wave spectra with a upper frequency limit, f_{max}, of 0.95 Hz, whereas most of the buoy observations have $f_{max} \simeq 0.4$ Hz. For fetch-limited wind seas, the mismatch in f_{max} will lead to a bias of about -0.3 s (3%) in $T_{0,2}$ (Text S2 and Figure S2). Similarly to H_s, model errors are larger in coastal regions: for example, the random error in the vicinity of the U.S. west coast and Australian coast on average is 0.12 and 0.17, respectively. Wave period along the Chinese coast is severely underestimated ($|b_n| > 20\%$), featuring the largest *RMSE* ϵ (>1.5 s) and *SI* (>0.15).

The temporal homogeneity of the ST6 wave hindcast is screened in Figure 12, where both the forcing winds and wave height are compared against in-situ observations collected at sufficiently long-lived, deep-water buoys ($d > 500$ m and duration longer than 25 years) in the northeast Pacific and northwest Atlantic (Figure 12f). Error statistics for the 41-years ERA5 U_{10} and ST6 H_s relative to the altimeter observations of Ribal and Young (2019) in this specific domain ($180° - 70°W, 15° N - 60° N$) are also overlaid for comparison. The plots clearly illustrate the pronounced seasonal variability of these error metrics for both winds and waves (see also Bidlot et al., 2002; Chawla et al., 2013). We will, however, mostly focus on the yearly moving averages in the following discussion. For the wind forcing, the ERA5 U_{10} yields a bias fluctuating between -0.5 and 0.3 m s^{-1} prior to 1990 (Figure 12a), likely because of rather limited buoys selected for the analysis (Fig-
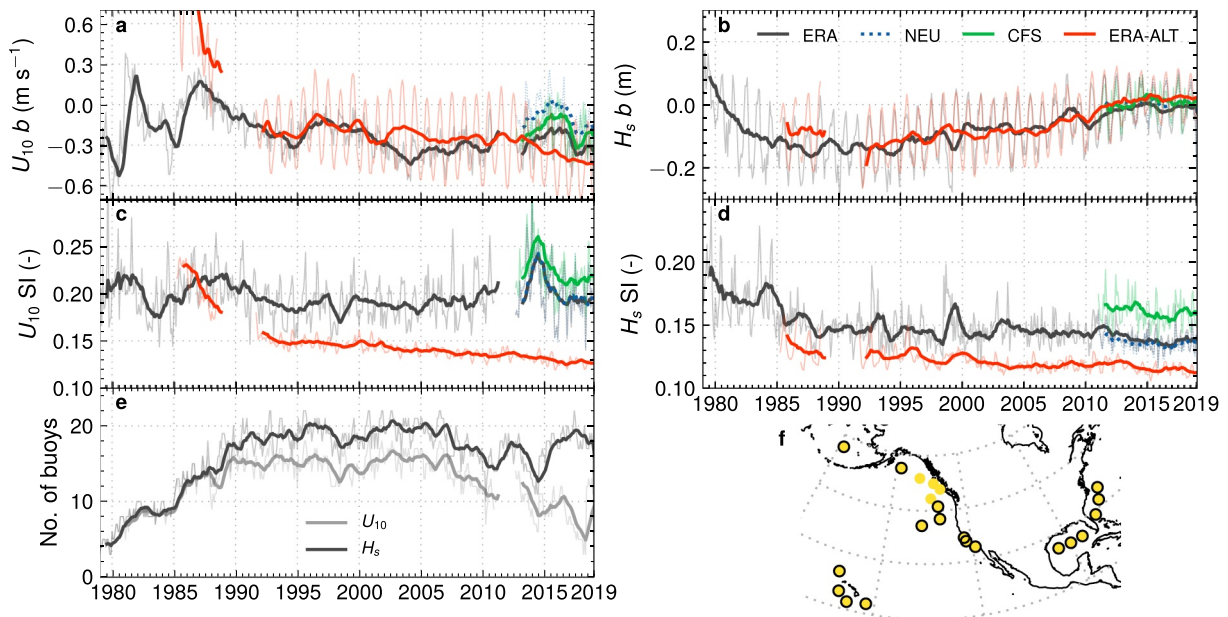
Figure 12. Errors of the reanalysis winds and corresponding ST6 wave hindcasts relative to buoy observations. (a) bias of U_{10}, (b) bias of H_s, (c) SI of U_{10}, and (d) SI of H_s, (e) number of buoys used in the analysis [only deep-water buoys ($d \geq 500$ m) with H_s records longer than 25 years are selected] and (f) locations of these buoys (a filled circle with black outline denotes both U_{10} and H_s records are reported at this specific location; otherwise only H_s is available). (a)–(d) black/blue/green lines: the ERA5 conventional winds U_{10}/neutral winds $U_{10,\mathrm{neu}}$/NCEP climate forecast system (CFS) U_{10} or the corresponding wave hincast. The red lines represent errors of the ERA5 conventional U_{10} and the resulting ST6 H_s relative to altimeters from Ribal and Young (2019) for the northeast Pacific and northwest Atlantic (180° − 70°W, 15° N − 60° N). Thin and thick lines in (a)–(e) denote monthly statistics and yearly moving averages.

ure 12e). Later, the negative bias seems to gradually increase until 2005 and becomes relatively stable from 2005 onwards (roughly −0.3 m s^{-1}). These biases are generally comparable to those from the altimeters, especially for years after 1992. It should be noted that the buoy U_{10} observations were assimilated into the ERA5 reanalysis (Hersbach et al., 2020, their section 5.3) and likely into the CFS (Stopa & Cheung, 2014), and therefore should not be regarded as an independent reference. This also explains why the buoy-based SI in U_{10} does not change much over the past four decades (~ 0.2; Figure 12c). On the contrary, the altimeter-based SI presents an evident downward trend. In line with results shown in Section 3.3, the CFS winds and the ERA5 $U_{10,\mathrm{neu}}$ are slightly stronger than the ERA5 U_{10}, and the CFS winds produce the largest random error; the two ERA5 winds perform very closely in terms of SI.

Compared against the American and Canadian buoys, the 41-years ST6 hindcast provides a bias in H_s gradually decreasing from about 8 cm in 1980 to approximately −15 cm in 1990 (Figure 12b). The H_s bias then starts increasing over the period from 1990 through 2010, subsequently reaching a relatively steady, almost unbiased value. Furthermore, the seasonal variability of the H_s bias is slightly reduced during 2010–2019. It should be emphasized that these biases are in excellent agreement with those from altimeters. In combination with Figure 10, these results clearly illustrate that the CCI altimeter data overestimate wave height from buoys slightly during the most recent years (e.g., from 2010 onwards), as stated in Dodet et al. (2020). Both the buoy- and altimeter-based SI suggests a continuous improvement in model performance with time, the magnitude of which noticeably differs by 3% (e.g., 0.14 vs. 0.11 in 2019; Figure 12d). Once again, for years since 2011, the CFS-based run yields the largest error (SI ~ 0.16); the run forced by the ERA5 $U_{10,\mathrm{neu}}$ is marginally better than that driven by the ERA5 conventional winds. Similar analyses performed for other geographical regions are presented in Appendix B.

5.2. One-Dimensional Wave Spectrum

Unlike conventional integral wave parameters (e.g., H_s, $T_{0,2}$), a detailed evaluation of the simulated wave spectra is less straightforward for lack of standard objective statistical measures, as summarized by Chawla et al. (2013). Here we analyze the modeled spectral shape in two ways: (a) use the diagnostic tool introduced
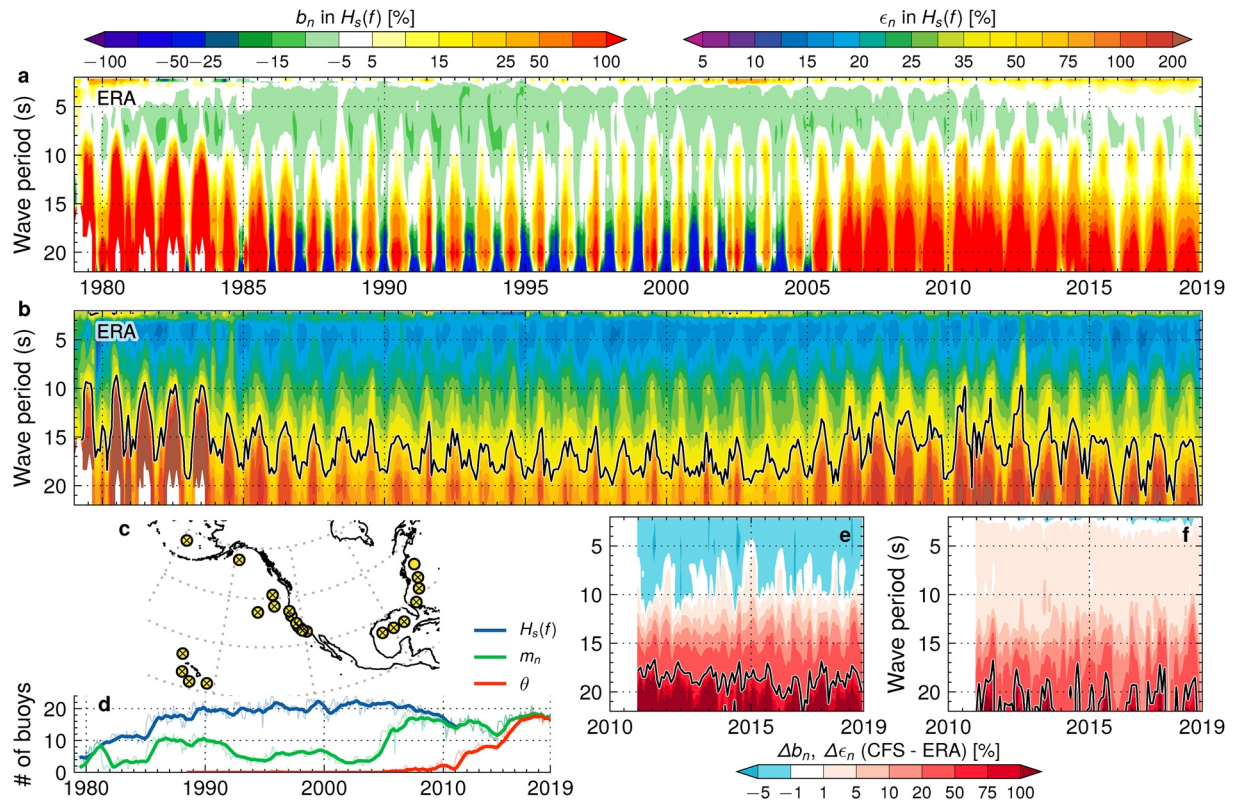
Figure 13. Comparison between the simulated wave spectra from the 41-years ST6 hindcast and the buoy observations: (a) normalized bias b_n and (b) *RMSE* ϵ_n of the equivalent wave height $H_s(f_i)$ as a function of wave period ($1/f_i$) and time. The black line in (b) highlights the contour line $\epsilon_n = 50\%$. (c) Locations of buoys used in the analysis (only buoys with $d \geq 300$ m and H_s records longer than 20 years are selected); markers without cross denote buoys without directional spectra. (d) number of the buoys used for calculating (blue) $H_s(f_i)$, (green) spectral moments and (red) directional properties. (e and f) the differences in b_n and ϵ_n between the ERA5-and CFS-based runs from 2011 onwards. Similarly, black lines highlight $\Delta b_n = 50\%$ and $\Delta\epsilon_n = 50\%$.

in Janssen (2004) and Janssen and Bidlot (2018) and calculate the frequency/period-dependent error statistics, and ii) focus on spectral moments of different orders which represent different wave physical properties (Ardhuin et al., 2009, 2010). Only observations provided by the U.S. NDBC buoys (Figure 13c) are used in these spectral analyses.

5.2.1. Frequency-Dependent Wave Height

Following Bidlot et al. (2007), the modeled spectrum was smoothed by averaging over three consecutive model frequency bins; we can then define the "equivalent" wave height for a given frequency bin as

$$H_s(f_i) = 4\sqrt{\int_{f_{l,i}}^{f_{h,i}} \mathcal{E}(f_i)\mathrm{d}f}, \tag{5}$$

where $\mathcal{E}(f)$ denotes the 3-bin moving averaged wave spectrum, $f_{l,i}$ and $f_{h,i}$ are the lower and upper boundaries of a given frequency bin, respectively. The buoy spectra were first interpolated onto the model frequency grid and then converted to $H_s(f_i)$ in the same way as we did for the model spectra.

The spectral bias b_n and *RMSE* ϵ_n of the 41-years ST6 hindcast as a function of wave period and time are presented in Figures 13a and 13b. We can observe the strong seasonality of the model performance particularly over the period from 1985 to 2005, during which the low-frequency wave energy (e.g., $T > 15$ s) is considerably overestimated in boreal summer ($b_n \sim 50 - 75\%$) and then significantly underestimated in boreal winter ($b_n \sim -25\%$). We note that during this specific period, the ERA5-based H_s underestimates buoy values by 10–15 cm (Figure 12b). When the H_s is more accurately estimated ($b \sim 0$ m) during more recent years (2011–2019), the low-frequency wave energy becomes more seriously overestimated ($b_n \sim 75 - 100\%$). This largely results from the known drawback of the DIA approach used for estimating the nonlinear transfer S_{nl},

that is, the DIA tends to push too much energy to the low-frequency end (e.g., Rogers & van Vledder, 2013). Liu et al. (2019) demonstrated that using a more accurate (but also more expensive) parameterization for S_{nl}, that is, the generalized multiple DIA proposed by Tolman (2013), could reduce positive biases in the low-frequency wave energy considerably (from 90% down to 20%; see their Figure 16). Compared against the large errors in these low-frequency bins ($\epsilon_n > 50\%$), model errors for shorter waves (e.g., $T < 10$ s) are much lower ($| b_n | < 10\%$ and $\epsilon_n \sim 12 - 20\%$; see also Figure 10 of Bidlot et al., 2007). For years after 2011, the CFS-based run generally presents relatively larger errors for all the wave periods except for the very short waves ($T < 3$ s; Figures 13e and 13f). A striking feature is that for very long waves (e.g., 20 s), ϵ_n from the CFS run could be approximately 50% higher than the ERA5-based values. In this regard, the differences in the two ERA5 runs (U_{10} and $U_{10,neu}$) are marginal (as can be expected from Figures 8d and 12d) and therefore are not shown.

5.2.2. High-Order Spectral Moments

Following the work by Ardhuin et al. (2009, 2010), three wave parameters based on different spectral moments are chosen here, including the significant surface orbital velocity U_{orb}, non-directional surface Stokes drift $U_{ss,nd}^c$ and mean square slope $\langle s_c^2 \rangle$, given by

$$U_{orb} = 2\left[\int_{f_{min}}^{f_c} \omega^2 E(f)df \right]^{1/2} = 4\pi\sqrt{m_2(f_c)} \simeq \pi H_s / T_{0,2}, \tag{6}$$

$$U_{ss,nd}^c = 4\pi \int_{f_{min}}^{f_c} kfE(f)df = 16\pi^3 m_3(f_c) / g, \tag{7}$$

$$\langle s_c^2 \rangle = \int_{f_{min}}^{f_c} k^2 E(f)df = 16\pi^4 m_4(f_c) / g^2. \tag{8}$$

Here the superscript or subscript "c" denotes that wave spectra are integrated up to a cut-off frequency f_c to obtain the n-th order spectral moment $m_n(f_c) = \int_{f_{min}}^{f_c} f^n E(f)df$; the deep water dispersion relation $\omega^2 = gk$ is assumed in Equations 7 and 8. In our calculations, $f_c = 0.44$ Hz was universally applied to the buoy and model spectra. Buoys deployed prior to 2005 usually had a maximum sampling frequency less than f_c (e.g., 0.33 Hz). We have simply excluded such buoy observations from our analysis and consequently, the number of buoys used to obtain $m_n(f_c)$ is significantly lower than that for calculating $H_s(f_i)$ (Equation 5; see Figure 13d for the comparison).

Comparison between the observed and modeled Stokes drift and mean square slope are summarized in Figure 14. We first show the buoy $U_{ss,nd}^c$ and $\langle s_c^2 \rangle$ during 2011–2019 as a function of wind speed U_{10} and wave height H_s (Figures 14a and 14d), clearly demonstrating that these two parameters generally increase with increasing wind and wave forcing, as reported by previous studies (e.g., Ardhuin et al., 2009, 2010). Our ST6 hindcasts reproduce the dependence of $U_{ss,nd}^c$ and $\langle s_c^2 \rangle$ on wind and waves remarkably well (Figures 14b and 14e) except that the variability of mean square slope with H_s at high winds ($U_{10} > 15$ m s^{-1}) is slightly underestimated. More direct comparisons for these two high-order spectral moments are illustrated in Figures 14c and 14f), from where we can see the ST6 hindcast forced by the ERA5 U_{10} agrees well with buoys in specifying the third and fourth moments. For the non-directional Stokes drift (a surrogate for m_3; Equation 7), the ST6 hindcast yields a correlation coefficient of 0.94 and SI of 0.25 (Figure 14c). Errors for the mean square slope (a surrogate for m_4; Equation 8) are slightly larger, corresponding to a ρ of 0.92 and SI of 0.28. These values are generally comparable to those reported by Ardhuin et al. (2009) and Rascle and Ardhuin (2013), where the authors used another source term package (i.e., ST4) for their simulations. It should also be mentioned that when taking into account wave directionality, the model performance for estimating the surface Stokes drift can be further improved (see Appendix C of Ardhuin et al., 2009).

The monthly normalized bias and SI for $U_{ss,nd}^c$ and $\langle s_c^2 \rangle$ are further presented in Figures 14g and 14h. Also shown are the metrics for U_{orb}, H_s and $T_{0,2}$. Compared against $U_{ss,nd}^c$ and $\langle s_c^2 \rangle$, the other parameters based on lower-order spectral moments are more homogeneously represented in time by the 41-years ST6 hindcast. Nonetheless, model performance for all the wave parameters are fairly steady after 2005, at least in terms of SI, partially because of the relatively steady number of the selected buoys (green line in Figure 13d). It
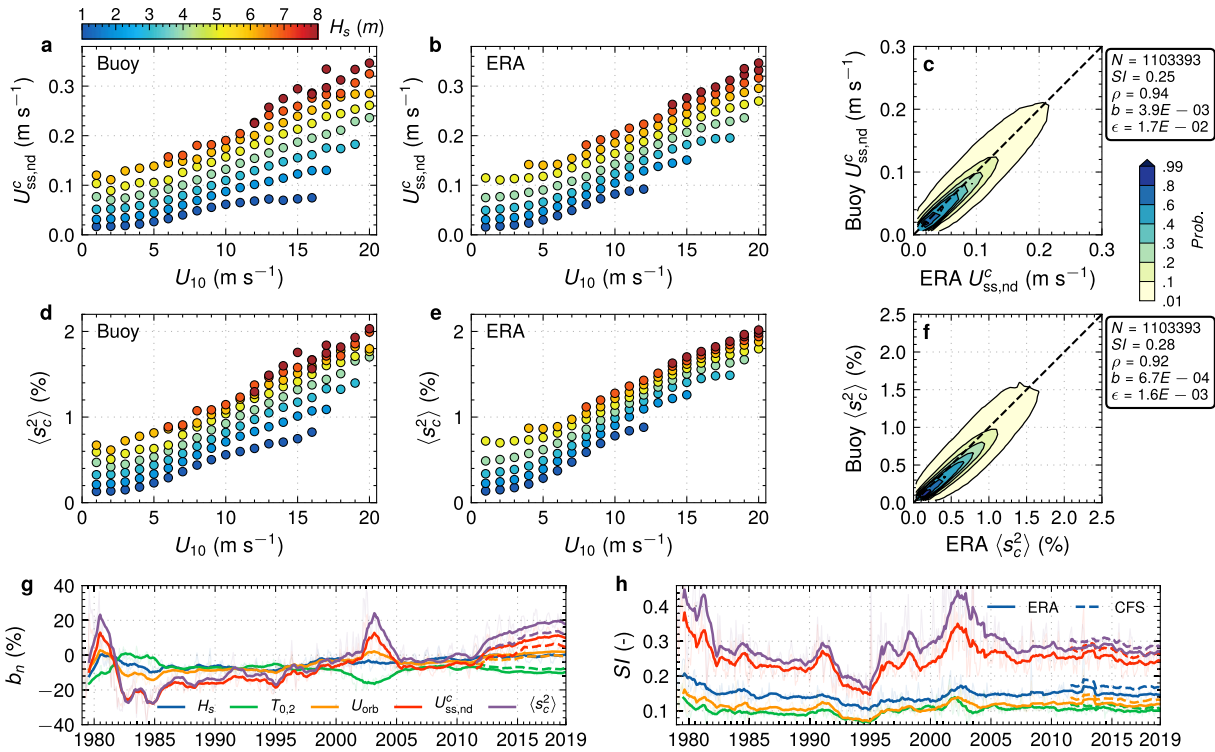
Figure 14. (a and b) averaged non-directional Stokes drift $U_{ss,nd}^c$ and (d and e) mean square slope $\langle s_c^2 \rangle$ in each 1 m s^{-1} bin of U_{10} and each 1 m bin of H_s according to (a and d) buoy observations and (b and e) the ST6 hindcast forced by ERA5 U_{10} during 2011–2019. The superscript or subscript "c" highlights that a cut-off frequency $f_c = 0.44$ Hz was taken for integrating wave spectra. (c and f) Direct comparison of $U_{ss,nd}^c$ and $\langle s_c^2 \rangle$ between buoy and hindcast for the same data shown in (a, b, d, and e). (g and h) Evolution of the normalized bias (b_n) and scatter index SI (thin line: monthly; thick line: yearly moving average) for wave height H_s, mean period $T_{0,2}$, significant surface orbital velocity U_{orb}, non-directional Stokes drift $U_{ss,nd}^c$ and mean square slope $\langle s_c^2 \rangle$ from ST6 wave hindcasts (solid line: run with the ERA5 conventional winds U_{10}; dashed line: the NCEP climate forecast system (CFS)-based run). Only the U.S. National Data Buoy Center (NDBC) buoys with $d \geq 300$ m, $f_{max} \geq f_c$ Hz and H_s records longer than 20 years are selected for analysis (see the green line in Figure 13d).

is seen that for the ERA5-based run after 2005, among the five wave parameters considered, $T_{0,2}$ shows the lowest random errors ($SI = 0.1$), closely followed by the U_{orb} with $SI \sim 0.12$. The error in H_s is slightly larger (0.14) but evidently much lower than errors for the high-order moments. As expected, the CFS-based run always shows slightly larger SI for these wave parameters. The normalized bias b_n for H_s shown here (blue line in Figure 14g) is generally consistent with the pattern of the absolute bias we show in Figure 12b, although significantly less buoys are used here as previously explained. That is, H_s is approximately underestimated by 8% during 1985–1995; but a gradual improvement is observed since then and H_s becomes nearly unbiased during 2010–2019. We note that for these recent years, when H_s is accurately estimated, $U_{ss,nd}^c$ and $\langle s_c^2 \rangle$ are overestimated roughly by 12% and 20%, respectively. Apart from errors owing to the forcing winds and model physics, another possible reason for this marked over-prediction of the high-order moments is that the 3 m discus NDBC buoys tend to underspecify the high-frequency energy at $f > 0.3$ Hz, as limited by the buoy response function (Rogers, 2017).

5.3. Wave Directionality

The last characteristic of the wave field to be evaluated here is the directionality, in terms of the mean wave direction θ_w and directional spread σ_θ (Kuik et al., 1988):

$$a_1 = \int_{f_{min}}^{f_c} \int_0^{2\pi} \cos\theta F(f,\theta) \mathrm{d}f \mathrm{d}\theta, \tag{9}$$
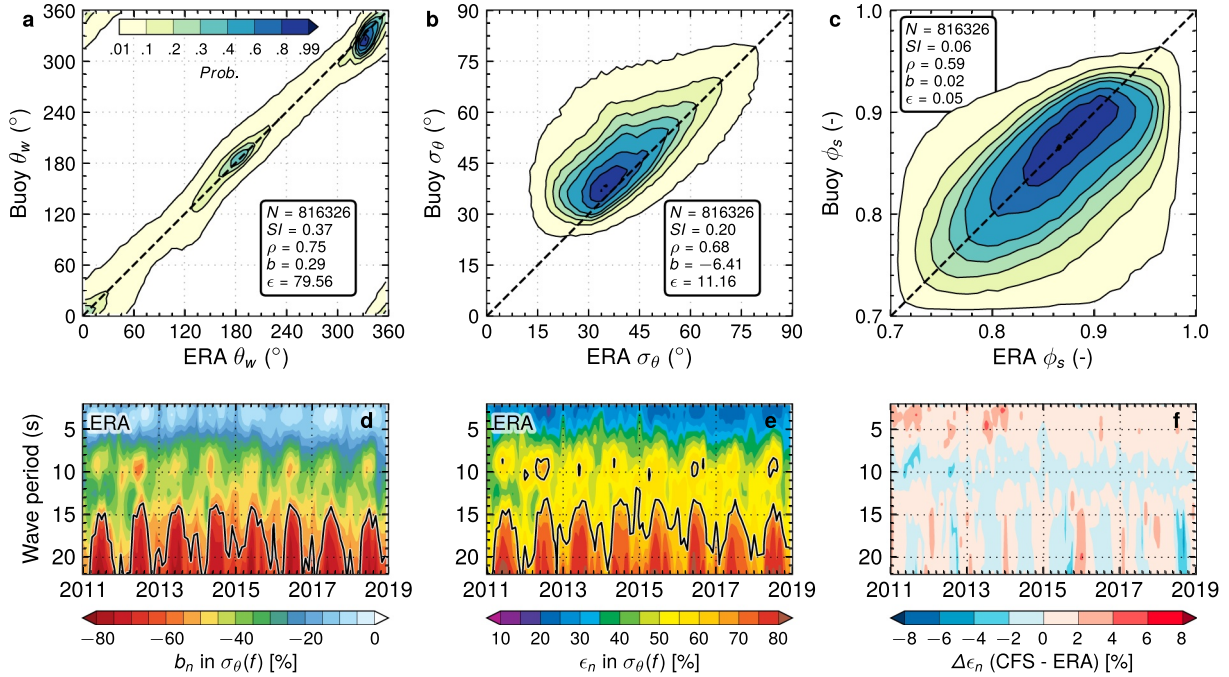
Figure 15. Comparison of the (a) mean wave direction θ_w, (b) directional spreading σ_θ, and (c) wave-spreading factor ϕ_s between buoy observations and the ST6 hindcast forced by the ERA5 conventional U_{10} during 2011–2019. (d and e) Normalized bias b_n and $RMSE$ ϵ_n of the frequency-dependent $\sigma_\theta(f)$ as a function of wave period and time; black lines highlight $b_n = -60\%$ or $\epsilon_n = 60\%$. (f) the differences in ϵ_n of $\sigma_\theta(f)$ between the ERA5-and NCEP climate forecast system (CFS)-based runs. Note that error metrics shown in Figure 15a is less meaningful because of the circular nature of directions.

$$b_1 = \int_{f_{\min}}^{f_c} \int_0^{2\pi} \sin\theta F(f,\theta) \mathrm{d}f \mathrm{d}\theta, \tag{10}$$

$$\theta_w = \arctan(b_1 / a_1), \tag{11}$$

$$\sigma_\theta = \sqrt{2\left(1 - \sqrt{(a_1^2 + b_1^2) / m_0^2}\right)}, \tag{12}$$

where $F(f,\theta)$ is the two-dimensional spectrum. A frequency-dependent directional spread $\sigma_\theta(f)$ can be defined in a similar way (WW3DG19).

Figure 15 demonstrates that the mean wave direction θ_w is fairly well-predicted (Figure 15a) by the ERA5-forced ST6 hindcast with most of data points lying in the vicinity of the 1:1 line. By contrast, the hindcast is less skillful in simulating the directional spread (Figure 15b; $\rho = 0.68$ and $b = -6°$), consistent with the results in Liu et al. (2019, their Figure 14). A close inspection of errors in $\sigma_\theta(f)$ in Figures 15d and 15e suggests that similar to the equivalent wave height $H_s(f)$, errors generally increase with wave period and are largest at low-frequency bins: $b_n < -60\%$ and $\epsilon_n > 60\%$ for $T > 15$ s. The CFS-based run shows comparable (but slightly larger) directional errors (Figure 15f).

It is worth mentioning that although the DIA is known to overestimate the integral directional spread σ_θ (S. Hasselmann et al., 1985), it is, meanwhile, inclined to underestimate the directional spread at low frequencies (i.e., $\sigma_\theta(f)$), as shown in Figure 9 of Liu et al. (2019). Furthermore, Smit and Janssen (2019) demonstrated that the scattering of wave rays by submesoscale eddies (ubiquitously present in the ocean) may broaden the directional distribution of ocean swells considerably. These two factors are likely important reasons for large directional errors at low-frequency bins.
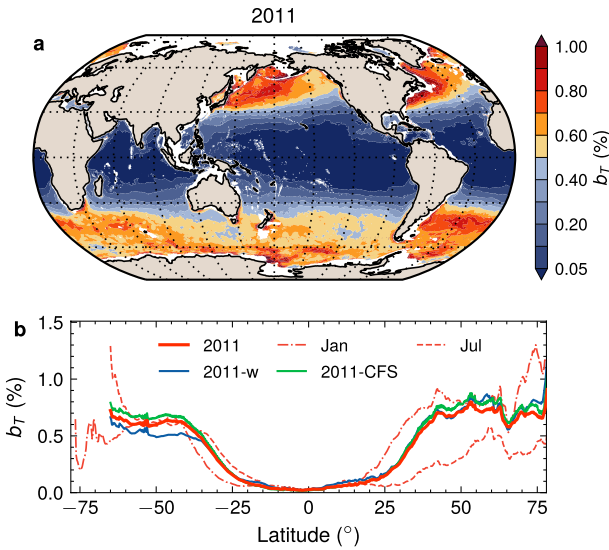
Figure 16. (a) global distribution of the breaking probability for dominant waves, b_T, averaged over 2011. Grid points with water depth less than 1,000 m are excluded from analysis. (b) Zonal averages of b_T: (solid red line) annual mean for 2011, (dash-dotted and dashed red lines) January and July; (blue) annual mean based on the watershed partitioning algorithm. The green line shows the annual mean of b_T based on the CFS-forced run. Note that except for the blue line, all the results are based on the partitioning scheme formulated by Equation 15.

6. Novel Wave Parameters

In this section, we will describe the unconventional wave parameters available in our wave hindcasts. Unless otherwise specified, we will only present results from the ST6 hindcast forced by the ERA5 conventional U_{10}.

6.1. Dominant Wave Breaking Probability

Banner et al. (2000) and Babanin et al. (2001) reported that the breaking probability for dominant surface waves b_T is strongly correlated with the significant wave steepness, a measure of the mean nonlinearity of dominant waves. According to Babanin et al. (2001, their Figure 12), b_T can be empirically estimated by

$$b_T = 85.1 \left[(\epsilon_{p,w} - 0.055)(1 + H_{s,w} / d) \right]^{2.33}, \tag{13}$$

where $\epsilon_{p,w}$ is the significant steepness of the spectral peak, given by

$$\varepsilon_{p,w} = 2 \left[\int_{0.7 f_{p,w}}^{1.3 f_{p,w}} E_w(f) \mathrm{d}f \right]^{1/2} k_{p,w}. \tag{14}$$

Here $k_{p,w}$ and $f_{p,w}$ are the peak wavenumber and frequency, respectively. The subscript "w" in the two equations above (e.g., $H_{s,w}$ and $E_w(f)$) means these quantities are computed from the wave spectrum $F(f, \theta)$ after filtering out any swell components (Banner et al., 2000). As in Bidlot (2001), we consider spectral components as wind seas if

$$\frac{c}{U_{10} \cos(\theta - \theta_u)} < \beta_w, \tag{15}$$

where $c = \omega / k$ is the phase velocity, θ_u is the wind direction, β_w is an empirical wind forcing parameter with $\beta_w \in [1.0, 2.0]$ used in the literature (e.g., Barstow et al., 2005). Here by default, we have chosen $\beta_w = 1.2$. An example for the evolution of b_T in a duration-limited test under constant U_{10} of 20 m s^{-1} has been provided in Liu et al. (2021, their Figure 2). We also explored the watershed algorithm internally available in WW3 for spectral partitioning (Hanson & Phillips, 2001; Tracy et al., 2007) and b_T calculated for the resulting wind sea partition using this approach was also archived.

Figure 16 presents the global distribution of the dominant wave breaking probability (Equations 13–15) averaged over the year 2011, also complemented by the zonal averages of b_T for the whole year and for January and July, respectively. The averaged b_T is fairly low in the equatorial zones with $b_T \leq 0.05\%$. Waves in these regions are predominated by swells with the wind sea fraction $\mathcal{W}_\mathcal{F}$ generally less than 20% (Appendix C; see also Semedo et al., 2011). Consequently, the wave slope would be very small and therefore dominant waves rarely break. Moving away from the equator, we see b_T increases almost quadratically with latitude ϕ for $|\phi| \in [10°, 40°]$. For ϕ beyond 40°, b_T does not change dramatically with ϕ, showing a value approximately of 0.7%. This is consistent with the fact that waves in midlatitude storm tracks (e.g., Southern Ocean) are more energetic, relatively younger and thus much steeper (Figures C1c, C1d, C1g and C1h). For the same reason, b_T in the northwest Pacific and Atlantic is noticeably higher than on the northeast side of these two basins, as illustrated by the northeastward directed contour line of $b_T = 0.5\%$. Results based on different spectral partitioning methods (blue line in Figure 16b) or from the CFS-based run (green line in Figure 16b) are quite similar. Figure 16b also suggests that the seasonal variation of b_T is remarkably greater in the Northern Hemisphere than in the Southern Hemisphere (red dashed-dotted and dashed lines), as expected from the seasonality of winds and waves (Figure C1; Semedo et al., 2011). It is noteworthy that the magnitude of the averaged b_T presented here is comparable to the satellite-based radiometric observations of whitecap fraction associated with actively breaking waves as reported by Salisbury et al. (2014). It is further noted that although the averaged b_T shown in Figure 16 generally is below 1%, significant variability about these mean values exists in the 3-hourly model outputs (not shown).

6.2. Wave-Induced Mixed Layer Depth

Turbulent mixing induced (generated or triggered) by ocean surface waves in the ocean surface boundary layer is a critical physical process which contributes significantly to the deepening of mixed layer (e.g., Babanin, 2006; McWilliams et al., 1997; Qiao et al., 2004). The notion of a non-breaking wave turbulence was first hypothesized by Babanin (2006) and subsequently supported by the laboratory experiments as reported in Babanin and Haus (2009). Starting from the concept of wave-amplitude-based Reynolds number (Re_w) defined for a monochromatic wave with the amplitude a and frequency $\omega = 2\pi f$,

$$\mathrm{Re}_w = \frac{aU_{\mathrm{orb}}}{\nu} = \frac{a^2\omega}{\nu}, \tag{16}$$

where ν is the kinematic viscosity of sea water, Babanin (2006) suggested that the orbital motion of ocean waves will generate turbulence when Re_w exceeds the critical wave Reynolds number $\mathrm{Re}_{\mathrm{cr}} \simeq 3000$. Since the amplitude a under a deep-water wavy surface decreases exponentially with increasing distance below the water surface (e.g., Young, 1999b),

$$\mathrm{Re}_w(z) \sim a(z)^2 \sim \exp(-2kz), \tag{17}$$

this implies a critical mixed layer depth (MLD) z_{cr} due to the wave-induced turbulence, below which the orbital wave motion will become laminar. According to Equation 16 and Equation 17, one can readily obtain

$$z_{\mathrm{cr}} = \frac{g}{2\omega^2} \ln \frac{a_0^2 \omega}{\nu \mathrm{Re}_{\mathrm{cr}}} \tag{18}$$

with a_0 the amplitude at the sea surface ($z = 0$). For oceanic, multi-scale wave fields, a_0 and ω are represented by the significant wave height H_s ($a_0 = 0.5H_s$) and peak frequency $\omega_p = 2\pi f_p$ (Babanin et al., 2009). The satellite-based, daily time-and-depth adjusted SST data from Merchant et al. (2019, Table 1) are used for computing the kinematic viscosity ν, following the empirical correlations of Sharqawy et al. (2010).

Figure 17 shows the climatological seasonal cycles of the derived wave-induced MLD z_{cr} and observations of MLD h_{ml} from de Boyer Montégut et al. (2004, density MLD; updated to include the data up to 2008). A close inspection of Figures 17c and 17d suggests that the spatial distribution of z_{cr}, to some extent, follows the patterns of peak wave period (or mean wave length; Figures C1e and C1f), demonstrating higher z_{cr} for longer waves. When compared against observations (Figures 17a and 17b), z_{cr} is comparable to h_{ml} in the North Pacific during DJF and in the Southern Ocean during JJA (purple '×' showing $z_{\mathrm{cr}} / h \in [0.75, 1.5)$). However, for most regions, z_{cr} overestimates h_{ml} considerably ($z_{\mathrm{cr}} / h > 1.5$; Figures 17c, 17d and 17f). We note that z_{cr} represents the asymptotic depth which would be achieved if waves of certain height and length persist long enough (tens of hours). In winter, storms are apparently long enough and this asymptotic depth is possibly achieved. But if the duration of the storm is short, the non-breaking wave-induced mixing is transient and the asymptotic z_{cr} is probably not reached.

6.3. Freak Wave Indexes

Over the past two decades, significant research efforts have been devoted to predicting the occurrence of freak waves within the spectral modeling framework (e.g., Benetazzo et al., 2015; Janssen, 2003; Mori et al., 2011). As one of the possible mechanisms leading to freak waves, third-order quasi-resonant four-wave interactions have been investigated extensively (e.g., Janssen, 2003; Onorato et al., 2009; Tulin & Waseda, 1999). In this context, the Benjamin-Feir index (BFI) is usually employed to indicate whether the underlying spectrum is unstable and thus favors freak wave occurrence.

For a given directional spectrum, Janssen (2003) and Janssen and Bidlot (2009) have defined the one-dimensional (1D) BFI as the ratio of the wave steepness $\varepsilon_p = 0.5H_s k_p$ to the spectral width δ_ω, given by

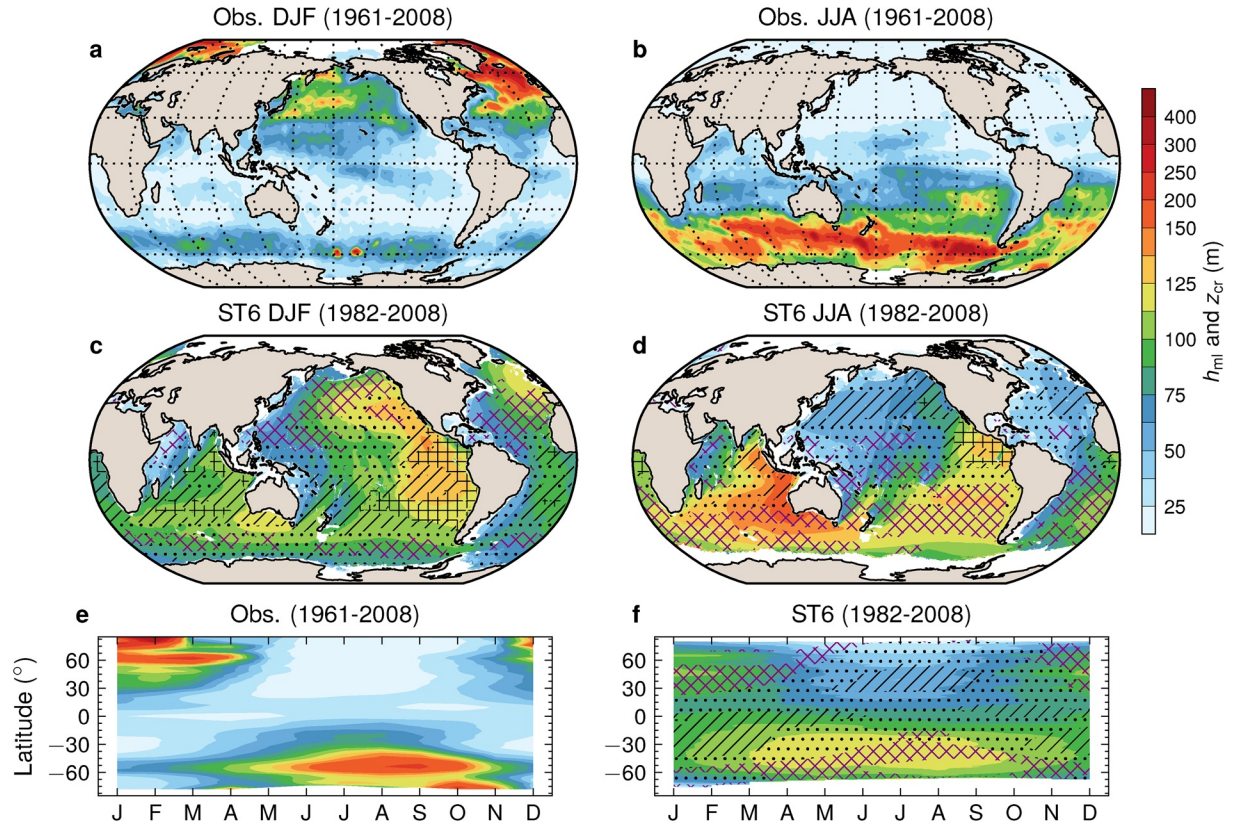$$\mathrm{BFI}_{1\mathrm{D}} = \frac{\varepsilon_p}{\sqrt{2}\delta_\omega}. \tag{19}$$

Figure 17. Climatology of the mixed layer depth: seasonal averages for (a and c) December–February (DJF) and (b and d) June–August (JJA). (a and b) observations of mixed layer depth (MLD) h_{ml} from de Boyer Montégut et al. (2004, updated to include the data up to 2008), (c and d) wave-induced MLD z_{cr} according to Equation 18. (e and f) Zonally averaged, seasonal cycles of the observed h_{ml} and modeled z_{cr}. Hatching in (c, d, and f) represents z_{cr} / h_{ml}: '×', '∙', '/' and '+' corresponding to z_{cr} / h_{ml} ∈ [0.75,1.5), < 3, < 5 and z_{cr} / h_{ml} ≥ 5, respectively.

In the narrow-band approximation, $\delta_\omega = (\sqrt{\pi} Q_p)^{-1}$ and Q_p is the Goda's spectral peakedness parameter (Goda, 2010):

$$Q_p = \frac{2}{m_0^2} \int f E^2(f) \mathrm{d}f. \tag{20}$$

To take into account the effect of directionality, Mori et al. (2011) suggested that the two-dimensional (2D) BFI can be estimated by

$$\mathrm{BFI}_{2D} = \frac{\mathrm{BFI}_{1D}}{\sqrt{1 + \xi_b R}} \quad \text{and} \quad R = \frac{\delta_\theta^2}{2\delta_\omega^2}, \tag{21}$$

where $\xi_b = 7.1$ is an empirical constant, $\delta_\theta = \sqrt{2(1 - M_1)}$ is a measure of the directional width (Janssen & Bidlot, 2009) and

$$M_1 = \frac{1}{m_0} \iint \cos\left[\theta - \theta_w(f)\right] F(f, \theta) \mathrm{d}f \mathrm{d}\theta, \tag{22}$$

in which $\theta_w(f)$ is a frequency-dependent mean wave direction, defined in a similar fashion as Equation 11. It is shown theoretically, numerically and experimentally that as the nonlinearity increases and the spectral and directional widths decrease (i.e., BFI_{2D} ↑), the probability of extreme waves will be amplified (e.g., Mori et al., 2011; Onorato et al., 2009).

Based on solutions of the Alber equation initialized by the JONSWAP spectrum, Ribal et al. (2013) proposed another set of freak wave indexes, defined as
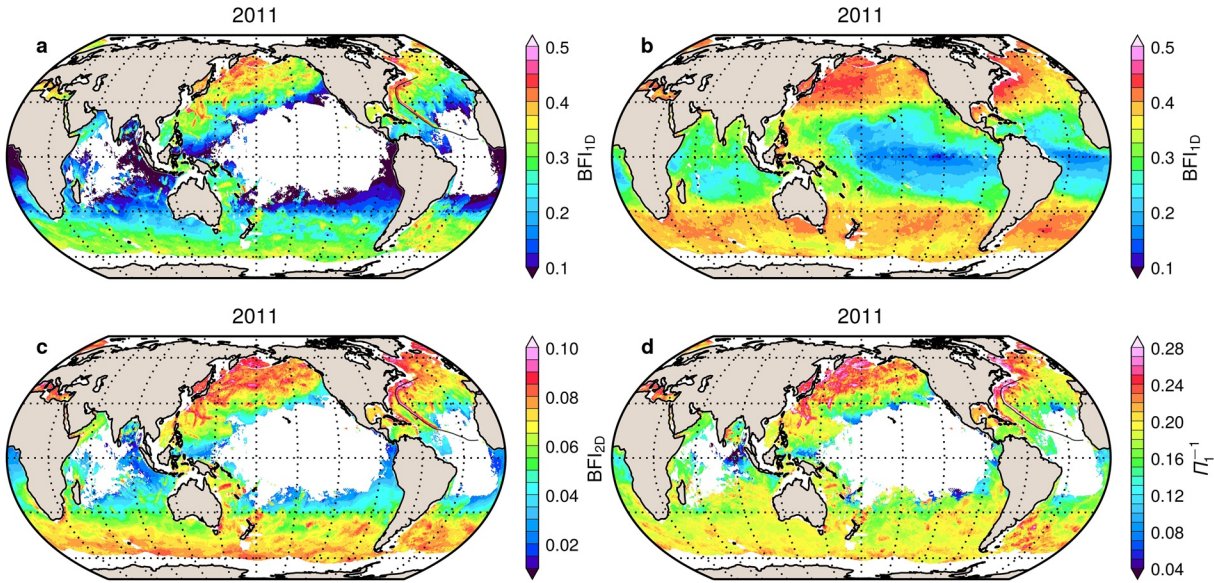
Figure 18. Global distribution of the 99th-percentile (a) BFI_{1D}, (c) BFI_{2D}, and (d) Π_1^{-1} calculated from wave spectra with a single wave system only over 2011. The black line in the North Atlantic shows the track of Hurricane Katia (2011). The track data were sourced from https://www.aoml.noaa.gov/hrd/hurdat/2011.html. (b) Same as (a) but for the 99th-percentile BFI_{1D} based on wind sea partitions at each grid point.

$$\Pi_1 = \frac{\varepsilon_p}{\alpha\gamma} \quad \text{and} \quad \Pi_2 = \Pi_1 + \frac{\xi_\pi}{\varepsilon_p A_p} \tag{23}$$

with α the high-frequency energy level and γ the peak enhancement factor of the JONSWAP form (Hasselmann et al., 1973). We used a piecewise fitting technique (Young & Verhagen, 1996) for determining α and γ for a given spectrum (see Text S3 for more details). A_p represents the directional narrowness parameter at the peak frequency introduced by Babanin and Soloviev (1998a, 1998b):

$$A_p^{-1} = \int_0^{2\pi} F(f_p, \theta) / \max\left[F(f_p, \theta)\right] d\theta. \tag{24}$$

Clearly, higher A_p indicates narrower directional width. Similar to ξ_b in Equation 21, ξ_π is an empirical constant ($O(10^{-2})$). We note that for the JONSWAP spectrum (Hasselmann et al., 1973, Equation S2), $\alpha \propto \varepsilon_p^2$ (Huang et al., 1981; Masson, 1993). Thus, $\Pi_1 \propto 1 / \varepsilon_p \gamma$; consequently the probability of extreme waves increases as Π_1 and Π_2 decrease.

Previous studies on the freak wave indexes described above (i.e., BFI_{1D}, BFI_{2D}, Π_1 and Π_2) were mainly limited to spectra with a single wave system (i.e., single peak). Wave fields in the real ocean are more complex and quite-often consist of multiple wave systems (e.g., in the low latitudes; Appendix C). It has also been suggested that the occurrence of extreme waves in crossing seas may result from different mechanisms (e.g., McAllister et al., 2019; Toffoli et al., 2011). In this regard, we have calculated the freak wave indexes separately for up to 3 wave systems (namely, wind sea, primary and secondary swells if applicable) existing in a given spectrum $F(f, \theta)$, based on the watershed partitioning scheme (Tracy et al., 2007). Figure 18 illustrates the spatial distribution of the 99th-percentile BFI_{1D}, BFI_{2D} and Π_1^{-1} over 2011. In Figures 18a, 18c and 18d, only wave spectra with a single wave system (i.e., unimodal) were included in the analysis. Accordingly, most regions at low latitudes are eliminated due to the prevalence of multiple wave systems (Figure C1). Clearly, these indexes are relatively high in the midlatitude storm tracks in both hemispheres and are highest in the northwest Pacific and Atlantic, primarily because of the relatively younger wave age (higher wind sea fraction; Figures C1g and C1h) and thus higher steepness. The footprint of a few storms, including Hurricane Katia (2011; highlighted as the black line), is also clearly visible in these figures, showing higher indexes on the right (stronger) side of hurricane tracks. Figure 18b demonstrates the 99th-percentile BFI_{1D} calculated for wind sea partitions only. The spatial patterns are comparable to those given in Figure 18a. We note that Figure 18 serves as an illustration of freak wave indexes available in our hindcast.

A thorough discussion of these indexes, including Π_2, over the past four decades will be reported elsewhere. It may also be worth mentioning that the space-time wave extremes estimated based on the linear and second-order wave theories (Barbariol et al., 2017; Benetazzo et al., 2015) were also archived in our data set and a detailed investigation of these extreme metrics will be pursued in the future.

6.4. Wave-Spreading Factor

The wave-spreading factor ϕ_s was introduced by Forristall and Ewans (1998). As an integrated measure, it represents the reduction in the in-line wave particle velocity due to directional spreading (Appendix D). For unidirectional waves ϕ_s is 1 and for omnidirectional waves $1/\sqrt{2}$; hence a lower ϕ_s indicates a directionally broader spectrum. Values of ϕ_s are widely desired for ocean engineering design. Forristall and Ewans (1998) analyzed a large ensemble of buoy observations and proposed specific values of ϕ_s for low-latitude monsoons, tropical and extratropical storms, respectively. Note that the rms directional spread σ_θ (Equations 9–12) is based on the first trigonometric moments of the directional spreading function, whereas the wave-spreading factor ϕ_s is based on the second moments (Appendix D). One is referred to Forristall and Ewans (1998) for discussions regarding the relation between σ_θ and ϕ_s.

The accuracy of the simulated ϕ_s from our hindcast is first checked against observations derived from the NDBC directional buoys in Figure 15c. Although the comparison is quite scattered, the simulated ϕ_s shows a good correlation with observations ($\rho = 0.6$), slightly lower than that for the directional spread σ_θ ($\rho \simeq 0.7$; Figure 15b). The global distribution of ϕ_s averaged over 1979–2019 is given in Figure 19a, demonstrating that ϕ_s is often low in the tropics (~ 0.8) due to the predominance of crossing swells or multi-modal wave systems, as manifested by the convergence of different wave directions, for example, in the equatorial Pacific (Figure C1c). In the mid latitudes, the spreading factor peaks in the vicinity of 30 - 35°N/S and then roughly decreases with increasing latitudes (see e.g., the blue line in Figure 19c). This is in good agreement with the observed behavior from Forristall and Ewans (1998, gray lines in our Figure 19c). The authors suggested that when moving toward high latitudes, the extratropical storms occur more frequently (their Figure 19); wave fields closer to storm centers would be much broader, as a result of rapidly changing winds (e.g., direction), than those farther from storm centers which usually evolve into long and directionally constrained swells. Accordingly, there is a clear latitudinal variation of ϕ_s in the storm tracks (ϕ_s is lower at higher latitudes; Figure 19c).

Selecting stormy sea states only ($H_s > 5$ m) from their observations, Forristall and Ewans (1998) empirically recommended $\phi_s \simeq 0.87 - 0.88$ for tropical cyclones and low-latitude monsoons. Our hindcast, averaged over 2011–2015 for spectra with H_s above 5 m, yields comparable estimate of ϕ_s in these regions (red dash-dotted lines in Figure 19c). For extratropical storms, our estimates (e.g., 90th-percentile) are lower than observations (gray dashed lines) at latitudes of 40° and biased high at higher latitudes (e.g., 70°). However, it should be mentioned that the observational sites analyzed by Forristall and Ewans (1998) were located closer to the coast and therefore might have not fully captured the latitudinal variability of ϕ_s. For example, the spreading factor off the west coast of the Americas and Australia is remarkably larger than in the central basins because of the presence of very long and directionally more focused swells (Figures 19a, C1e and C1f).

We also present the directional spread σ_θ (12) in Figures 19b and 19d, showing slightly more complex latitudinal variability. Regions with lower ϕ_s generally have larger σ_θ, as expected. The largest seasonality of σ_θ in the Northern Hemisphere appears at the extratropical storm tracks (e.g., 30-40° N; see the green and yellow dotted lines in Figure 19d), largely driven by the seasonal variation of winds (Figures C1a and C1b). The largest seasonality of σ_θ in the Southern Hemisphere, however, is present in the tropics (0°–15°S) because of the seasonal migration of the "swell front" at these regions, particularly in the central Pacific Ocean (Young, 1999a, our Figures C1c and C1d).

7. Discussion and Conclusions

In this study, we present global wave hindcasts developed using the third generation spectral wave model WW3 with the observation-based source terms (ST6; Liu et al., 2019) and a hybrid rectilinear-curvilinear IRI grid system ($\sim 0.25° \times 0.25°$, Figure 3; Rogers & Linzell, 2018). Three distinct global hindcasts are produced,

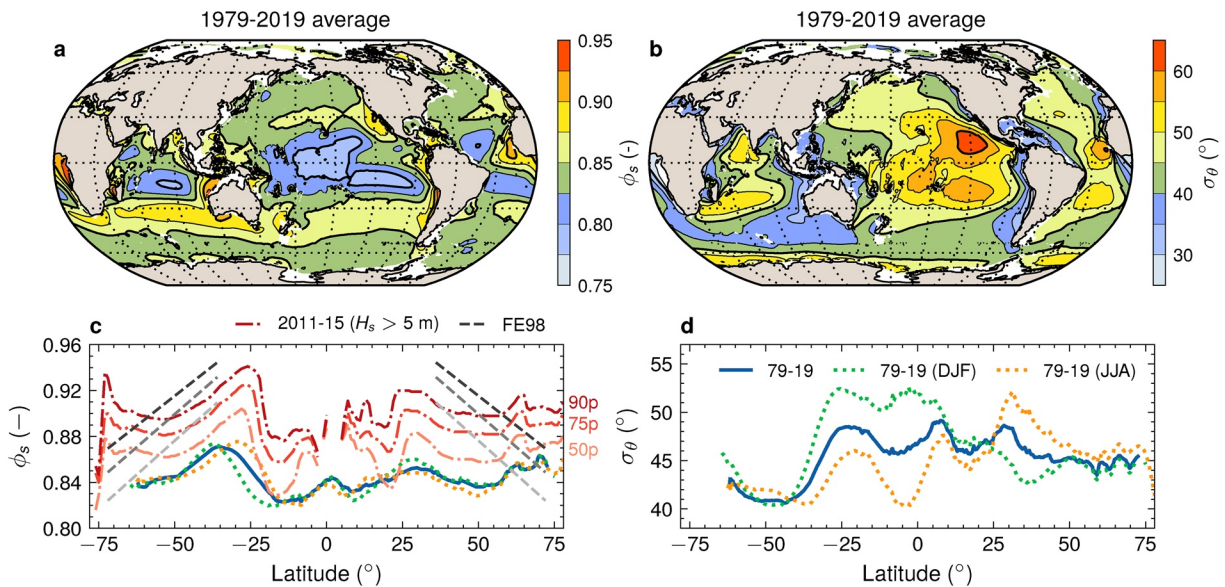**Figure 19.** (a) wave-spreading factor ϕ_s and (b) directional spread σ_θ calculated using the ST6 wave hindcast averaged over 1979–2019. (c and d) Zonal averages of ϕ_s and σ_θ: (blue solid line) averaged over 1979–2019, (green and yellow dotted lines) seasonal averages for December–February (DJF) and June–August (JJA). The red dash-dotted lines represent the 50th-, 75th- and 90th-percentiles of ϕ_s calculated for spectra with H_s above 5 m over the period 2011–2015. The gray dashed lines highlight the field observations analyzed by Forristall and Ewans (1998).

including (a) a long-term hindcast (1979–2019) forced by the ERA5 conventional U_{10} and (b) two short-term hindcasts (2011–2019) driven by the CFS U_{10} and the ERA5 neutral winds $U_{10,neu}$, respectively (Table 3). These simulations are validated against extensive in-situ buoy observations and satellite altimeter records (Figures 1 and 2). Apart from the conventional wave parameters (e.g., wave height H_s and wave period $T_{0,2}$), the modeled spectral shape is also thoroughly screened in terms of multiple spectral metrics, including the frequency-dependent wave height $H_s(f)$ (Janssen, 2004), spectral moments of different orders (Ardhuin et al., 2009, 2010) and wave directionality (Forristall & Ewans, 1998; Kuik et al., 1988). Novel wave parameters available in our hindcasts, namely the dominant wave breaking probability (Babanin et al., 2001), wave-induced mixed layer depth (Babanin, 2006), freak wave indexes (Janssen & Bidlot, 2009; Mori et al., 2011; Ribal et al., 2013) and wave-spreading factor (Forristall & Ewans, 1998), are further described and briefly discussed.

Key findings are summarized below:

1. Overall, the latest ERA5 reanalysis winds (0.25° × 0.25°) are in better agreement with the altimeter U_{10} measurements, in particular for the most recent years (e.g., from 2010 onward; Figures 4 and 6). Nevertheless, the ERA5 U_{10} tends to underestimate extreme winds ($U_{10} > 18$ m s^{-1}; Figures 4d and 4f), sharing the similar limitation with its predecessor (i.e., ERA-Interim; Rascle & Ardhuin, 2013). Compared against the conventional U_{10}, the ERA5 neutral winds $U_{10,neu}$ performs marginally better on the west side of Pacific and Atlantic (Figure 5d). The CFS winds (0.5° × 0.5°), although providing slightly weaker skills, represent extreme winds significantly better, as previously reported by Chawla et al. (2013) and Stopa and Cheung (2014). It is also demonstrated that the performance of the ERA5 U_{10} evolves more homogeneously with time (Figure 6), which stands as another reason why we selected the ERA5 U_{10} for the long-term ST6 hindcast.

2. The ST6 wave hindcasts forced by these different winds, once calibrated through the wind stress parameter (CDFAC), agree remarkably well with altimeter H_s records (Figures 7–9). Controlled by the accuracy of winds, the ERA5-based ST6 hindcasts noticeably outperform the CFS-based runs in terms of bulk error statistics (e.g., $SI \sim 0.12$ vs 0.14 in 2011). In the Southern Ocean, the CFS-based run overestimates H_s by 4%–8% in 2011. Such overestimation is clearly improved in the ERA5-based runs. But unsurprisingly, the CFS-based wave hindcast matches extreme sea states (e.g., $H_s > 10$ m) considerably better (Figures 7d and 7f). The ERA5 $U_{10,neu}$-based runs again show marginally lower errors in the northwest Pacific and Atlantic (Figure 8d) than the ones forced by the ERA5 conventional U_{10}.

3. Relative to the altimeter data set of Ribal and Young (2019), our long-term ERA5-based wave hindcast shows inhomogeneous biases evolving with time, changing the sign from negative to positive around 2010 (Figure 9a). This, however, primarily arises from the systematic differences in H_s across distinct altimeter missions, especially for the ENVISAT and JASON-1/2. Our hindcast performs more steadily when compared against the CCI altimeter data set (Figure 10), in which H_s from the former three altimeters are more consistent (Dodet et al., 2020). Figure 10 also explains why another ERA5-based wave hindcast (CY46R1) yields a more consistent (i.e., more positive) H_s trend with the CCI data set than with the data set of Ribal and Young (2019), as recently reported by Timmermans et al. (2020, their Figure 3). Nonetheless, these results do not indicate that one altimeter data set outperforms another. It instead highlights the inconsistency in altimeter H_s arising from different calibration methodology, as we have explained in Section 4. It is futher shown in Figure 12b that our model biases relative to the data set of Ribal and Young (2019) are actually well supported by those derived from in-situ NDBC buoy observations. All these discrepancies (Figures 9a, 10 and 12b) seem to imply possible inhomogeneity in NDBC buoy measurements, which calls for further investigations of these various wave data sets (see also Ardhuin et al., 2019).

4. Compared against the collected global buoy data set, the long-term ST6 hindcast forced by the ERA5 U_{10} shows very promising performance in open waters. Moving closer to the coasts, model skills clearly decline, and the largest error is seen in the East China and Yellow Seas where buoys are located in fairly shallow waters (see also Figure 8b). Consistent with the altimeter-based comparisons, the ERA5-forced runs performs slightly better than the CFS-forced run when verified against the buoy measurements, in particular for representing the peak period T_p (Figure B3).

5. Careful examination of the modeled spectral shape suggests that our wave hindcasts generally agree well with buoy observations in specifying the high-frequency wave energy and high-order spectral moments (e.g., $U_{ss,nd}^c$ and $\langle s_c^2 \rangle$; Figures 13 and 14). Nonetheless, errors in the low-frequency wave energy are quite significant, especially for frequency bins with $T > 15$ s ($\epsilon_n > 50\%$; Figure 13b). Such errors are largely attributed to the drawback of the DIA approach used for estimating the nonlinear transfer S_{nl}, and adopting more accurate S_{nl} parameterizations (e.g., Tolman, 2013) would, to a large extent, resolve this problem (Liu et al., 2019; Rogers & van Vledder, 2013). It is further illustrated that for very long waves ($T > 18$ s), the CFS-based run yields considerably larger errors than the ERA5-based hindcasts (Figures 13e and 13f). This seems consistent with the result that the CFS-forced run presents larger errors in the Southern Ocean (Figure 8) which is an expansive source region for very long swells arriving at the U.S. west coast (Collard et al., 2009; Snodgrass et al., 1966). The hindcasts are less skillful in estimating the wave directionality (in terms of σ_θ and ϕ_s; Figure 15). Similarly, the errors of σ_θ increase with wave periods, reaching more than 60% for b_n and ϵ_n when $T > 15$ s (Figures 15d and 15e).

6. The breaking probability for dominant surface waves b_T (Babanin et al., 2001) is fairly low in tropics with the annual mean for 2011 less than 0.05% (Figure 16). When moving away from the equator, b_T almost increases quadratically with latitudes until 40° N/S with the annual mean of about 0.7% in the midlatitude storm tracks. We note that b_T however is highly variable in space and time due to the intermittent nature of wave breaking. The global distribution of the nonbreaking wave-induced mixed layer depth z_{cr} (Babanin, 2006), to some extent, follows the spatial patterns of the mean wave length (Figures 17, C1e and C1f). It is seen that z_{cr} is comparable to the observations of MLD (de Boyer Montégut et al., 2004) in the North Pacific during DJF and in the Southern Ocean during JJA; for the remaining regions and seasons, z_{cr} however is considerably higher than measurements. The climatology of the wave-spreading factor ϕ_s is in good agreement with observations of Forristall and Ewans (1998), and, thus, will be useful for future ocean engineering design (Figure 19). Meanwhile, it is observed that the greatest seasonality of the directional spread appears at the equatorial zone 0°-15° S due to the seasonal migration of "swell front" in these regions (Figures 19d, C1c and C1d). A preliminary analysis of freak wave indexes is also presented in Figure 18 and more thorough discussion will be reported separately.

In conclusion, having seen the promising performance of the ST6 wave hindcasts in specifying multiple wave parameters (e.g., H_s, $T_{0,2}$, U_{orb}, $U_{ss,nd}^c$, $\langle s_c^2 \rangle$), we believe these data will be highly useful for wave climate research, ocean/coastal engineering design, remote sensing applications and atmosphere-wave-ocean coupling modeling. Furthermore, these data sets, together with global wave hindcasts developed previously (e.g., Bidlot et al., 2019; Chawla et al., 2013; Fan et al., 2012; Rascle & Ardhuin, 2013), will form a

large ensemble of realizations of historical evolution of sea states simulated with distinct wave physics and wind forcing, which will help quantify sea states in real oceans more accurately. Significant errors in the low-frequency bins for both $H_s(f)$ and $\sigma_\theta(f)$ may provide guidance for further wave model development. Inter-comparsion among existing wave hindcasts is beyond the scope of the paper and will be pursued in the future.

Appendix A: ECMWF In-Situ Observation Data Set

The bulk of the data gathered by ECMWF (Bidlot, 2017) came from its operational archive, where all data distributed via the Global Telecommunication System (GTS) are kept. The data come from moored buoys, with the exception of data from operating platforms in the North and Norwegian Seas and the Gulf of Mexico. The main data providers are the US, via the NDBC and CDIP, Canada, the UK, France, Ireland, Norway, Iceland, Germany, Spain, Brazil, and South Korea. Coauthors A. Semedo, J. Bidlot, and G. Lemos blended the data set with four other regional data sets, around Australia (from Integrated Marine Observing System), Portugal mainland and the Azores archipelago (from Instituto Hidrográfico and the CLIMAAT project - Clima e Meteorologia dos Arquipélagos Atlânticos), the Baltic Sea (from CMEMS - Copernicus Marine Environment Monitoring System) and Brazil (from PNBOIA). In this paper, we have used a subset of this data set only, particularly for buoys/platforms located in the northeast Atlantic and Mediterranean Sea (Figure 2).

Appendix B: Further Validation Against Satellite and In-Situ Observations

B1. Upper Percentile Winds and Waves

The time series of the upper percentile (i.e., 90, 95 and 99th-percentiles) reanalysis winds, normalized by the corresponding altimeter measurements of Ribal and Young (2019), are given in Figure B1a, B1c and B1e. The CFS significantly overestimates these stronger winds by around 10% prior to 1993, then under-predicts the altimeter values by 2%–3% over the years 1995–2008, and eventually agrees well with observations after 2010. Comparable results for the CFS winds have been previously reported by Chawla et al. (2013, their Figure 5) and Stopa and Cheung (2014). The ERA5 provides comparable 95 and 99th-percentile values to the measurements from the early satellite missions (GEOSAT and ERS-1). Relative to the remaining altimeters, the ERA5 performs more homogeneously over time than the CFS. It underestimates the 90 and 95th-percentiles by approximately 5%, and the 99th percentile by roughly 8%. The scatter in the altimeter data at the 99th percentile is considerably larger than for lower percentiles (Figure B1a). As suggested by Figure 4, the ERA5 neutral winds are almost identical to the conventional winds at these upper percentiles, and therefore are not shown in Figure B1 for clarity.

The temporal evolution of the normalized upper percentile simulated wave height generally follows the pattern of the H_s biases (Figures B1b, B1d and B1f vs. Figure 9a). The computed 90 and 95th-percentile H_s from the ERA5 U_{10}-based run underestimates altimeter counterparts by less than 4% during 1992–2007 and then becomes almost unbiased after 2010; the 99th percentile is underestimated by 2%–5% throughout the altimeter era. The CFS-based run (dotted line in Figure B1) overestimates the 90 and 95th-percentile H_s roughly by 4% and is comparable to altimeter measurements at the 99th percentile. The reasons for the dissimilarity in patterns of the normalized upper percentile winds and waves are (a) that the altimeter U_{10} and H_s are determined separately based on different principles and (b) that errors in the reanalysis winds are partially canceled through calibrating the wind stress parameter CDFAC of the ST6 package (Table 3). Figure B1 also reveals that the CRYOSAT-2 and HY-2 are apparently inconsistent with other simultaneously flying missions in specifying extreme seas, especially for the 99th-percentile H_s. Liu et al. (2016) demonstrated that using a two-branch (first- or second-degree polynomial) function, rather than the linear calibration formula as adopted by Ribal and Young (2019), for correcting CRYOSAT-2 and HY-2 H_s records would mostly resolve these problems.
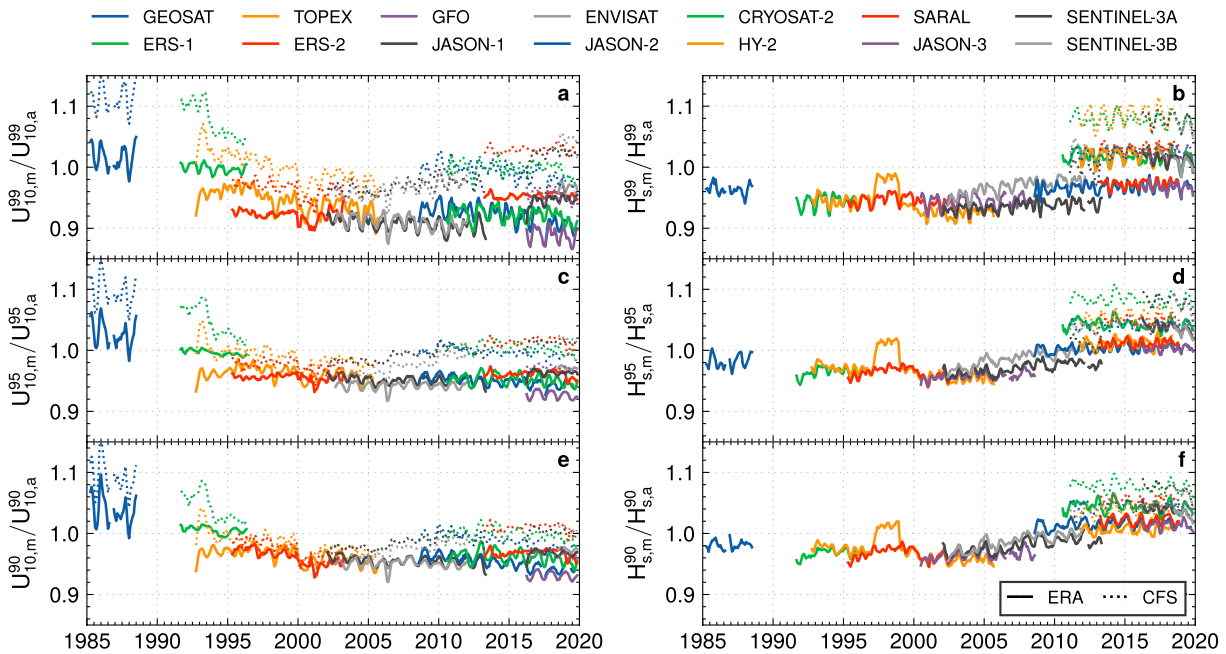
Figure B1. Normalized (a, c and e) U_{10} (solid: ERA5, dotted: CFS) and (b, d and f) H_s (solid and dotted lines denote WW3-ST6 hindcasts forced by the ERA5 and CFS U_{10}, respectively) at (a and b) 99th, (c and d) 95th and (e and f) 90th percentiles for the global domain. Results with the ERA5 neutral winds $U_{10,neu}$ are very close to those for the ERA5 U_{10}, and therefore are not shown here for clarity.

B2. Regional Analysis

Analyses similar to those presented in Figure 12 are further performed for three other regions, namely the northeast Atlantic, the coastal region around the Korean Peninsula and the Australian east coast, where the available buoy records are relatively large in size and sufficiently long in time (Figure B2). Only H_s is analyzed and the minimum data duration y_{min} and water depth d_{min} used for filtering buoys are described in the figure caption. We first discuss the performance of the 41 years ST6 hindcast forced by the ERA5 conventional U_{10}. Among these regions, the Australian coastal buoy observations are the most homogeneous in time (Figures B2e and B2f), showing a H_s bias very close to 0 m throughout the four decades except for the period from 1985 to 1995 ($b \sim -10$ cm), and a relatively uniform SI around 0.25. Nearly all the buoys chosen in the northeast Atlantic are located in the northern North Sea (Figure B2a) with water depth in between 100 and 150 m, at which waves are primarily deep-water waves (e.g., van Vledder et al., 2016). The corresponding SI from both buoys and altimeters (0.14 and 0.1 in 2019; Figure B2b) is comparable to those shown in Figure 12d for the northeast Pacific and northwest Atlantic. Nonetheless, the buoy-based bias presents remarkable interannual variability (Figure B2a), ranging from about −15 to 0 cm. Meanwhile, the negative biases from altimeters are noticeably greater (10–20 cm difference) prior to 2014. The largest H_s errors are seen around the Korean Peninsula: the SI from buoys is apparently large (0.5) during 1996–2007 but is significantly reduced after 2009 (roughly 0.3); wave height is moderately overestimated by about 15 cm during the former period and then underestimated by around 10 cm over the latter period (Figures B2c and B2d). It should be noted that only a few buoys are selected for the regional analysis in the northeast Atlantic and in the Korean coastal waters during their respective early stages (e.g., prior to 2005; Figures B2a and B2c). Inclusion of new buoys at a later stage might have significantly affected the temporal homogeneity of the buoy-based error statistics. For all the three regions, biases from the comparison with buoy and altimeter measurements become more consistent during the later years since 2010. The SI from altimeters is always remarkably lower than the buoy-based values. This is primarily because the altimeter observations are more distant from coastlines (altimeter records less than 50 km offshore are excluded) and correspond to a considerably larger spatial extent (as indicated in the caption of Figure B2). For years after 2011, the CFS-based run shows slightly larger random errors in H_s than the ERA5-based runs in the northeast Atlantic and near the Korean coast.
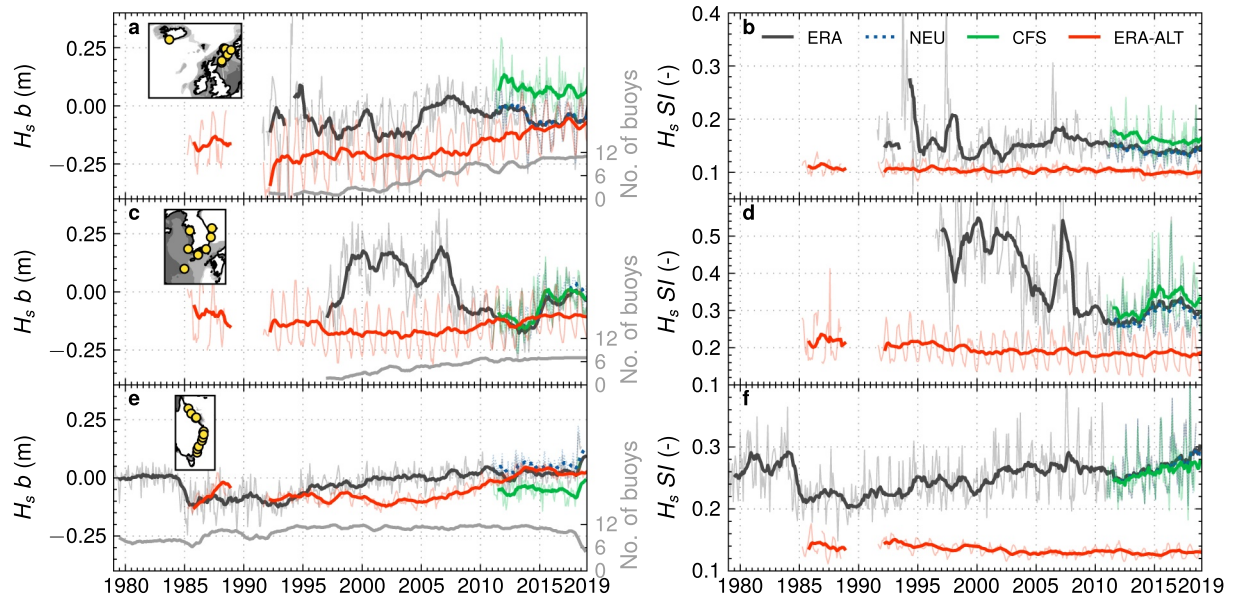
Figure B2. Similar to Figure 12 but for (left) bias and (right) *SI* of H_s at three other regions: (a and b) northeast Atlantic ($d_{min} = 100$ m, $y_{min} = 10$ yr), (c and d) coastal area around the Korean Peninsula ($d_{min} = 0$ m, $y_{min} = 10$ yr), (e and f) eastern Australian coastal waters ($d_{min} = 0$ m, $y_{min} = 25$ yr). Only buoys with $d \geq d_{min}$ and H_s records longer than y_{min} yr are selected. The number of the selected buoys is shown as the gray line (yearly moving average) in the left panels and their locations are presented in the insets (gray shaded contour is the same as Figure 11). Color scheme for error statistics is the same as Figure 12. Errors from altimeters (red lines) are calculated for the domain: (a and b) northeast Atlantic ($25° W - 5°E, 57° N - 64° N$), (c and d) coastal region around the Korean Peninsula ($122° E - 132°E, 30° N - 40° N$) and (e and f) eastern Australian coast ($140° E - 158°E, 45° S - 10° S$).

A more comprehensive inter-comparison of the ST6 wave hindcasts from 2011 onwards, forced by three distinct winds, is summarized in Figure B3. Buoys are sorted into different groups by their geographical locations (see the figure caption). It can be seen that for all the parameters (U_{10}, H_s, $T_{0,2}$ and peak period T_p), the ERA5-based results are slightly better than the CFS-based ones, and such outperformance is most pronounced in the comparison of T_p (Figure B3d). Consistent with Bidlot et al. (2002), the model skill in predicting T_p is noticeably lower than for other parameters (e.g., $\rho \sim 0.7$) because (a) T_p itself is fairly noisy (discontinuous) and (b) when multiple wave systems coexist (a common situation in the ocean; Appendix C), accurately estimating T_p would require a reasonable prediction of the relative strength of these coexisting systems and of their respective peak locations, which is a more challenging task. Differences arising from the usage of two ERA5 winds (U_{10} and $U_{10,neu}$) are not easily detectable in this figure.
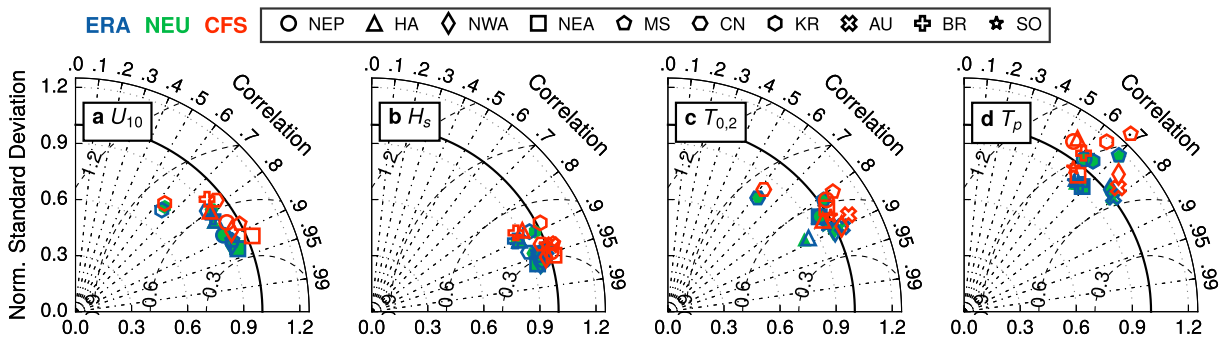

Figure B3. Taylor diagrams summarizing the comparison between ST6 wave hindcasts (from 2011 onwards) and buoys at different regions: NEP (northeast Pacific, $170° E - 115° W, 30° N - 65° N$), HA (Hawaii, $165° W - 150° W, 15° N - 26° N$), NWA (northwest Atlantic, $100° W - 40° W, 10° N - 55° N$), NEA (northeast Atlantic, $25° W - 15° W, 46° N - 66° N$), MS (Mediterranean Sea), CN (Chinese coast), KR (Korean Peninsula), AU (Australian coast), BR (Brazilian coast), SO (Southern Ocean). See also Figure 2 for these buoy locations. (a) wind speed U_{10}, (b) wave height H_s, (c) mean wave period $T_{0,2}$ and (d) peak wave period T_p.

Appendix C: Wind and Wave Climatology

The climatology of global winds and waves, calculated using the ERA5 conventional U_{10} and our ST6 wave hindcast over 1979–2019, is presented in Figure C1. Averages for two seasons, that is, December–February (DJF) and July–August (JJA), are shown to illustrate the seasonal variability of these parameters.

In the boreal winter (DJF; Figure C1a), U_{10} maximizes in the extra-tropical storm tracks in the North Atlantic (~ 12 m s^{-1}). Winds at the midlatitude North Pacific is slightly lower (about 11 m s^{-1}). The tropical oceans generally show the lowest U_{10}, particularly for the equatorial Indian Ocean, western Pacific and eastern Atlantic (approximately 4 m s^{-1}). High winds occur throughout the Southern Ocean westerlies with U_{10} in between 9 and 11 m s^{-1}. During the austral winter (JJA; Figure C1b), winds in the North Pacific and Atlantic
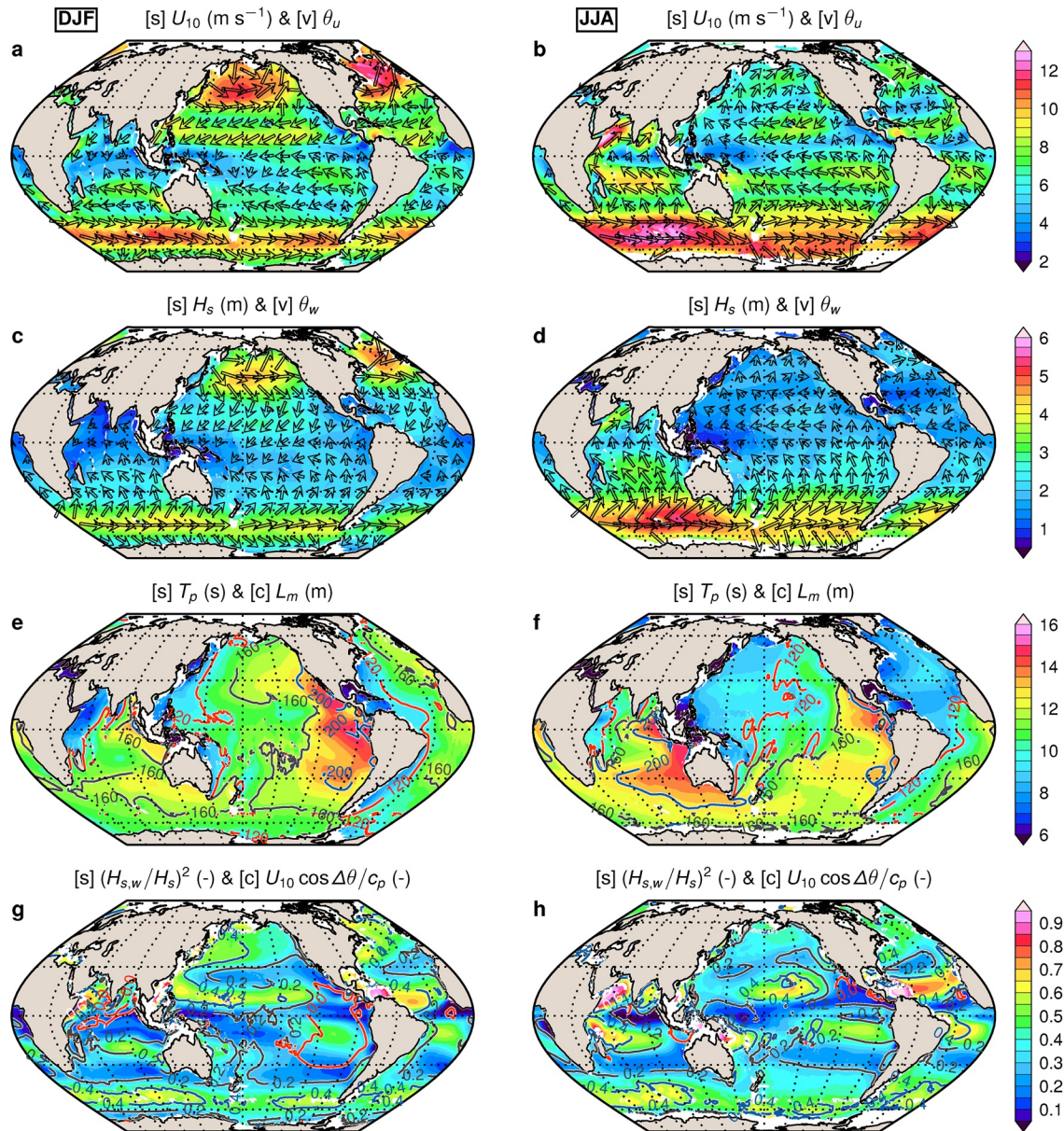
Figure C1. Wind and wave climatology calculated using the ST6 wave hindcast over 1979–2019: (left) seasonal averages for December–February (DJF) and (right) for June–August (JJA). (a and b) (shading) wind speed U_{10} and (vector) wind direction θ_u; (c and d) (shading) significant wave height H_s and (vector) mean wave direction θ_w; (e and f) (shading) peak wave period T_p and (contours) mean wave length L_m; (g and h) (shading) wind sea fraction $(H_{s,w}/H_s)^2$ and (contours) inverse wave age $U_{10}\cos\Delta\theta / c_p$.

are much reduced (8 m s^{-1}). The maximal U_{10} of about 13 m s^{-1} is observed in the southern Indian Ocean and off the coast of Somalia (due to the low-level southwesterly Somali jet).

The global distribution of wave height H_s generally follows the patterns of wind speed (Figures C1c and C1d), showing energetic waves in the North Pacific and Atlantic storm tracks ($H_s > 4$ m) in DJF and in the Southern Ocean all year round. The highest averaged H_s is seen in the area to the south of the Indian Ocean (between Australia and South Africa; $H_s \sim 5.5$ m). A remarkable feature is that winds and waves are often misaligned (in terms of wind direction θ_u and mean wave direction θ_w) at the low-latitude edge of storm tracks ($\phi \sim 40°$) and on the east side of ocean basins, especially for the area off the west coast of Americas in low latitudes.

The seasonal averages of the peak wave period T_p are given in Figures C1e and C1f). Also shown are the mean wave length, defined by

$$L_m = \frac{2\pi}{m_0} \int k^{-1} E(f) \mathrm{d}f. \tag{C1}$$

Unlike the strong latitudinal pattern of the U_{10} and H_s distributions, there is a distinct meridional variation in T_p and L_m with the highest values occurring in the tropical and subtropical eastern Pacific during DJF and in the eastern Indian Ocean during JJA ($T_p \sim 15$ s and $L_m > 200$ m). Waves are generally shorter ($T_p < 10$ s and $L_m < 120$ m) on the west side of ocean basins because of limited fetch. Waves in the Southern Ocean have $T_p \sim 11 - 13$ s and L_m around 160 m.

We further present the seasonal averages of the wind sea fraction $\mathcal{W}_{\mathcal{F}} = (H_{s,w} / H_s)^2$ and inverse wave age $\mathcal{W}_{\mathcal{A}}^{-1} = U_{10} \cos(\theta_u - \theta_w) / c_p$ in Figures C1g and C1h), where $H_{s,w}$ is the wind sea wave height based on the watershed partitioning (Tracy et al., 2007) and c_p is the peak phase velocity, given by $c_p = g / 2\pi f_p$ for deep-water waves. These figures clearly demonstrate the dominance of swells in the global oceans, as previously reported by, for example, Hanley et al. (2010) and Semedo et al. (2011). Only a few regions correspond to $\mathcal{W}_{\mathcal{F}} > 50\%$ and $\mathcal{W}_{\mathcal{A}}^{-1} > 0.4$, including the northwest Pacific and Atlantic during DJF, the subtropical trade wind regions and the Southern Ocean storm tracks. The wind sea fraction $\mathcal{W}_{\mathcal{F}}$ is very low in tropics ($< 20\%$) due to the low wind speed and prevalence of swells propagating from the midlatitude storm tracks. The inverse wave age $\mathcal{W}_{\mathcal{A}}^{-1}$ becomes below zero (red contour in Figure C1g) in the eastern tropical Pacific during DJF primarily because of the misalignment of swells and local winds.

The brief description of the global wind and wave climatology is presented here to facilitate our discussions in Section 6. For more thorough investigations of wind and wave climate in global basins, the reader is referred to Gulev and Grigorieva (2006), Hanley et al. (2010), Semedo et al. (2011), and Young (1999a), among others.

Appendix D: Wave-Spreading Factor

The wave-spreading factor of Forristall and Ewans (1998) is estimated by the following steps. Starting from the two-dimensional spectrum $F(f,\theta)$, we get the normalized directional spreading function $D(f,\theta)$ by

$$D(f,\theta) = F(f,\theta) / E(f). \tag{D1}$$

We then have the second-order trigonometric moments of the spreading function $a_2(f)$ and $b_2(f)$ (e.g., Kuik et al., 1988):

$$a_2(f) = \int_0^{2\pi} \cos(2\theta) D(f,\theta) \mathrm{d}\theta, \tag{D2}$$

$$b_2(f) = \int_0^{2\pi} \sin(2\theta) D(f,\theta) \mathrm{d}\theta. \tag{D3}$$

The variance and covariance of the u and v components of the wave particle velocity at zero lag and integrated over depth are given by integrating the second trigonometric moments of $D(f,\theta)$ over frequency and weighted by the frequency spectrum $E(f)$:

$$\alpha_{uu}^2 = \frac{1}{2}\int E(f)\big[1 + a_2(f)\big]\mathrm{d}f, \tag{D4}$$

$$\alpha_{vv}^2 = \frac{1}{2}\int E(f)\big[1 - a_2(f)\big]\mathrm{d}f, \tag{D5}$$

$$\alpha_{uv}^2 = \frac{1}{2}\int E(f)b_2(f)\mathrm{d}f. \tag{D6}$$

Performing a coordinate system transformation from (x, y) to (a, b) in which the velocity components are statistically independent (i.e., $\alpha_{ab} = 0$) (by using the principal wave direction θ_p), we will have

$$\alpha_{aa}^2 = \frac{1}{2}(\alpha_{uu}^2 + \alpha_{vv}^2) + r, \tag{D7}$$

$$\alpha_{bb}^2 = \frac{1}{2}(\alpha_{uu}^2 + \alpha_{vv}^2) - r, \tag{D8}$$

$$r^2 = \frac{1}{4}(\alpha_{uu}^2 - \alpha_{vv}^2)^2 + (\alpha_{uv}^2)^2. \tag{D9}$$

In the new coordinate system (a, b), the velocity in the principal wave direction is normally distributed with the standard deviation of α_{aa}. Similarly, for unidirectional waves, the velocity distribution has a standard deviation of $\alpha = \sqrt{\alpha_{uu}^2 + \alpha_{uv}^2}$. The wave-spreading factor ϕ_s is thus defined by the reduction of the rms velocity in the principal wave direction due to directional spreading of wave field, given by

$$\phi_s = \alpha_{aa}/\sqrt{(\alpha_{uu}^2 + \alpha_{vv}^2)}. \tag{D10}$$

For unidirectional waves ϕ_s is 1 and for omnidirectional waves $1/\sqrt{2}$, thus $\phi_s \in [1/\sqrt{2}, 1]$.

Data Availability Statement

The hindcasts are freely available and data access will be provided from Q. Liu (liuqingxiang@ouc.edu.cn; qingxiang.liu@unimelb.edu.au) and A. Babanin (a.babanin@unimelb.edu.au). A full list of wave parameters archived in these data sets and other technical details (i.e., how to download data) can be found in Liu and Babanin (2021, https://doi.org/10.5281/zenodo.4497717). While preparing the manuscript, the ST6 hindcasts forced by the ERA5 "back extension" data (1950–1978; preliminary version) were produced as well. All the reanalysis, satellite data sets and most of the in-situ buoy measurements used in this paper are publicly available as summarized in Tables 1 and 2.

References

Abdalla, S. (2012). Ku-band radar altimeter surface wind speed algorithm. *Marine Geodesy*, *35*, 276–298. https://doi.org/10.1080/01490419.2012.718676

Abdolali, A., Roland, A., Van Der Westhuysen, A., Meixner, J., Chawla, A., Hesser, T. J., et al. (2020). Large-scale hurricane modeling using domain decomposition parallelization and implicit scheme implemented in WAVEWATCH III wave model. *Coastal Engineering*, *157*, 103656. https://doi.org/10.1016/j.coastaleng.2020.103656

Ardhuin, F., Marié, L., Rascle, N., Forget, P., & Roland, A. (2009). Observation and estimation of lagrangian, stokes, and Eulerian currents induced by wind and waves at the sea surface. *Journal of Physical Oceanography*, *39*(11), 2820–2838. https://doi.org/10.1175/2009jpo4169.1

Ardhuin, F., Rogers, E., Babanin, A. V., Filipot, J.-F., Magne, R., Roland, A., et al. (2010). Semiempirical dissipation source functions for ocean waves. Part I: Definition, calibration, and validation. *Journal of Physical Oceanography*, *40*(9), 1917–1941. https://doi.org/10.1175/2010JPO4324.1

Ardhuin, F., Roland, A., Dumas, F., Bennis, A.-C., Sentchev, A., Forget, P., et al. (2012). Numerical wave modeling in conditions with strong currents: Dissipation, refraction, and relative wind. *Journal of Physical Oceanography*, *42*(12), 2101–2120. https://doi.org/10.1175/jpo-d-11-0220.1

Ardhuin, F., Stopa, J. E., Chapron, B., Collard, F., Husson, R., Jensen, R. E., et al. (2019). Observing sea states. *Frontiers in Marine Science*, *6*, 124. https://doi.org/10.3389/fmars.2019.00124

Babanin, A. V. (2006). On a wave-induced turbulence and a wave-mixed upper ocean layer. *Geophysical Research Letters*, *33*(20), L20605. https://doi.org/10.1029/2006GL027308

Babanin, A. V. (2011). *Breaking and dissipation of ocean surface waves*. Cambridge University Press.

Babanin, A. V., Ganopolski, A., & Phillips, W. R. (2009). Wave-induced upper-ocean mixing in a climate model of intermediate complexity. *Ocean Modelling*, *29*(3), 189–197. https://doi.org/10.1016/j.ocemod.2009.04.003

Babanin, A. V., & Haus, B. K. (2009). On the existence of water turbulence induced by nonbreaking surface waves. *Journal of Physical Oceanography*, *39*(10), 2675–2679. https://doi.org/10.1175/2009JPO4202.1

Babanin, A. V., & Soloviev, Y. P. (1998a). Field investigation of transformation of the wind wave frequency spectrum with fetch and the stage of development. *Journal of Physical Oceanography*, *28*(4), 563–576. https://doi.org/10.1175/1520-0485(1998)028<0563:fiotot>2.0.co;2

Babanin, A. V., & Soloviev, Y. P. (1998b). Variability of directional spectra of wind-generated waves, studied by means of wave staff arrays. *Marine and Freshwater Research*, *49*(2), 89–101. https://doi.org/10.1071/mf96126

Babanin, A. V., Young, I. R., & Banner, M. L. (2001). Breaking probabilities for dominant surface waves on water of finite constant depth. *Journal of Geophysical Research*, *106*, 11659–11676. https://doi.org/10.1029/2000JC000215

Banner, M. L., Babanin, A. V., & Young, I. R. (2000). Breaking probability for dominant waves on the sea surface. *Journal of Physical Oceanography*, *30*(12), 3145–3160. https://doi.org/10.1175/1520-0485(2000)030<3145:bpfdwo>2.0.co;2

Barbariol, F., Alves, J.-H. G., Benetazzo, A., Bergamasco, F., Bertotti, L., Carniel, S., & et al. (2017). Numerical modeling of space-time wave extremes using wavewatch iii. *Ocean Dynamics*, *67*(3–4), 535–549. https://doi.org/10.1007/s10236-016-1025-0

Barstow, S. F., Bidlot, J.-R., Caires, S., Donelan, M. A., Drennan, W. M., Dupuis, H., & Wyatt, L. R. (2005). *Measuring and analysing the directional spectrum of ocean waves* In D. Hauser, K. Kahma, H. Krogstad, S. Lehner, J. Monbaliu, & L. Wyatt (Eds.), COST office. Retrieved from https://hal.archives-ouvertes.fr/hal-00529755

Battjes, J. A., & Janssen, P. (1978). Energy loss and set-up due to breaking of random waves. In *Proceedings of 16th international conference on coastal engineering* (pp. 569–587). https://doi.org/10.1061/9780872621909.034

Belcher, S. E., Grant, A. L., Hanley, K. E., Fox-Kemper, B., Van Roekel, L., Sullivan, P. P., et al. (2012). A global perspective on langmuir turbulence in the ocean surface boundary layer. *Geophysical Research Letters*, *39*(18), L18605. https://doi.org/10.1029/2012gl052932

Benetazzo, A., Barbariol, F., Bergamasco, F., Torsello, A., Carniel, S., & Sclavo, M. (2015). Observation of extreme sea waves in a space–time ensemble. *Journal of Physical Oceanography*, *45*(9), 2261–2275. https://doi.org/10.1175/jpo-d-15-0017.1

Bidlot, J.-R. (2001). Ecmwf wave-model products. In ECMWF Newsletter (Vol. 91). European Centre for Medium-Range Weather Forecasts.

Bidlot, J.-R. (2017). Twenty-one years of wave forecast verification. *ECMWF Newsletter*, *150*, 31–36.

Bidlot, J.-R., Holmes, D. J., Wittmann, P. A., Lalbeharry, R., & Chen, H. S. (2002). Intercomparison of the performance of operational ocean wave forecasting systems with buoy data. *Weather and Forecasting*, *17*(2), 287–310. https://doi.org/10.1175/1520-0434(2002)017<0287:iotpoo>2.0.co;2

Bidlot, J.-R., Janssen, P., Abdalla, S., & Hersbach, H. (2007). *A revised formulation of ocean wave dissipation and its model impact* (Tech. Rep. No. ECMWF Tech. Memo. 509). ECMWF. Retrieved from http://www.ecmwf.int/publications/

Bidlot, J.-R., Lemos, G., & Semedo, A. (2019). *ERA5 reanalysis and ERA5 based ocean wave hindcast*. In 2nd international workshop on waves, storm surges and coastal hazards, incorporating the 16th international waves workshop.

Booij, N., Ris, R. C., & Holthuijsen, L. H. (1999). A third-generation wave model for coastal regions: 1. model description and validation. *Journal of Geophysical Research*, *104*(C4), 7649–7666. https://doi.org/10.1029/98jc02622

Breivik, Ø., Janssen, P. A., & Bidlot, J.-R. (2014). Approximate stokes drift profiles in deep water. *Journal of Physical Oceanography*, *44*(9), 2433–2445. https://doi.org/10.1175/jpo-d-14-0020.1

Caires, S., & Sterl, A. (2003). Validation of ocean wind and wave data using triple collocation. *Journal of Geophysical Research*, *108*(C3), 3098. https://doi.org/10.1029/2002jc001491

Carrasco, A., Semedo, A., Isachsen, P. E., Christensen, K. H., & Saetra, Ø. (2014). Global surface wave drift climate from era-40: The contributions from wind-sea and swell. *Ocean Dynamics*, *64*(12), 1815–1829. https://doi.org/10.1007/s10236-014-0783-9

Cavaleri, L., Abdalla, S., Benetazzo, A., Bertotti, L., Bidlot, J.-R., Breivik, Ø., et al. (2018). Wave modelling in coastal and inner seas. *Progress in Oceanography*, *167*, 164–233. https://doi.org/10.1016/j.pocean.2018.03.010

Cavaleri, L., Alves, J. H. G. M., Ardhuin, F., Babanin, A. V., Banner, M., Belibassakis, K., et al. (2007). Wave modelling - The state of the art. *Progress in Oceanography*, *75*(4), 603–674. https://doi.org/10.1016/j.pocean.2007.05.005

Cavaleri, L., Fox-Kemper, B., & Hemer, M. (2012). Wind waves in the coupled climate system. *Bulletin of the American Meteorological Society*, *93*(11), 1651–1661. https://doi.org/10.1175/bams-d-11-00170.1

Chawla, A., Spindler, D. M., & Tolman, H. L. (2013). Validation of a thirty year wave hindcast using the climate forecast system reanalysis winds. *Ocean Modelling*, *70*, 189–206. https://doi.org/10.1016/j.ocemod.2012.07.005

Chawla, A., & Tolman, H. L. (2008). Obstruction grids for spectral wave models. *Ocean Modelling*, *22*(1–2), 12–25. https://doi.org/10.1016/j.ocemod.2008.01.003

Chelton, D. B., Ries, J. C., Haines, B. J., Fu, L.-L., & Callahan, P. S. (2001). Satellite altimetry. In L.-L. Fu, & A. Cazenave (Eds.), Satellite altimetry and Earth sciences A handbook of techniques and applications (Vol. 69, pp. 509). Publisher.

Chelton, D. B., & Xie, S.-P. (2010). Coupled ocean-atmosphere interaction at oceanic mesoscales. *Oceanography*, *23*(4), 52–69. https://doi.org/10.5670/oceanog.2010.05

Collard, F., Ardhuin, F., & Chapron, B. (2009). Monitoring and analysis of ocean swell fields from space: New methods for routine observations. *Journal of Geophysical Research*, *114*(C7), C07023. https://doi.org/10.1029/2008jc005215

Cordero, S. G., Rogers, E., & Fan, Y. (2020). *Improvement of Wavewatch III output through a wind speed modification based in boundary layer temperature variability*. arXiv. Retrieved from arXiv:2005.02841.

de Boyer Montégut, C., Madec, G., Fischer, A. S., Lazar, A., & Iudicone, D. (2004). Mixed layer depth over the global ocean: An examination of profile data and a profile-based climatology. *Journal of Geophysical Research*, *109*(C12), C12003. https://doi.org/10.1029/2004jc002378

Doble, M. J., & Bidlot, J.-R. (2013). Wave buoy measurements at the Antarctic sea ice edge compared with an enhanced ECMWF WAM: Progress towards global waves-in-ice modelling. *Ocean Modelling*, *70*, 166–173. https://doi.org/10.1016/j.ocemod.2013.05.012

Dodet, G., Piolle, J.-F., Quilfen, Y., Abdalla, S., Accensi, M., Ardhuin, F., et al. (2020). The sea state CCI dataset v1: Towards a sea state climate data record based on satellite observations. *Earth System Science Data*, *12*(3), 1929–1951. https://doi.org/10.5194/essd-12-1929-2020

Donelan, M. A. (1990). Air-sea interaction. *The Sea*, *9*, 239–292.

Donelan, M. A. (1999). Wind-induced growth and attenuation of laboratory waves. In *Institute of mathematics and its applications conference series* (Vol. *69*, pp. 183–194).

Donelan, M. A., Babanin, A. V., Young, I. R., & Banner, M. L. (2006). Wave-follower field measurements of the wind-input spectral function. Part II: Parameterization of the wind input. *Journal of Physical Oceanography*, *36*(8), 1672–1689. https://doi.org/10.1175/JPO2933.1

Donelan, M. A., & Pierson, W. J. (1987). Radar scattering and equilibrium ranges in wind-generated waves with application to scatterometry. *Journal of Geophysical Research*, *92*(C5), 4971–5029. https://doi.org/10.1029/jc092ic05p04971

Fan, Y., Ginis, I., & Hara, T. (2009). The effect of wind–wave–current interaction on air–sea momentum fluxes and ocean response in tropical cyclones. *Journal of Physical Oceanography*, *39*(4), 1019–1034. https://doi.org/10.1175/2008jpo4066.1

Fan, Y., Lin, S.-J., Held, I. M., Yu, Z., & Tolman, H. L. (2012). Global ocean surface wave simulation using a coupled atmosphere–wave model. *Journal of Climate*, *25*(18), 6233–6252. https://doi.org/10.1175/jcli-d-11-00621.1

Forristall, G. Z., & Ewans, K. C. (1998). Worldwide measurements of directional wave spreading. *Journal of Atmospheric and Oceanic Technology*, *15*(2), 440–469. https://doi.org/10.1175/1520-0426(1998)015<0440:wmodws>2.0.co;2

Gemmrich, J., Thomas, B., & Bouchard, R. (2011). Observational changes and trends in northeast pacific wave records. *Geophysical Research Letters*, *38*(22), L22601. https://doi.org/10.1029/2011gl049518

Goda, Y. (2010). *Random seas and design of maritime structures* (3rd ed.,). World scientific.

Gulev, S. K., & Grigorieva, V. (2006). Variability of the winter wind waves and swell in the north atlantic and north pacific as revealed by the voluntary observing ship data. *Journal of Climate*, *19*(21), 5667–5685. https://doi.org/10.1175/jcli3936.1

Ha, K.-J., Nam, S., Jeong, J.-Y., Moon, I.-J., Lee, M., Yun, J., et al. (2019). Observations utilizing korea ocean research stations and their applications for process studies. *Bulletin of the American Meteorological Society*, *100*(10), 2061–2075. https://doi.org/10.1175/bams-d-18-0305.1

Hanley, K. E., Belcher, S. E., & Sullivan, P. P. (2010). A global climatology of wind–wave interaction. *Journal of Physical Oceanography*, *40*(6), 1263–1282. https://doi.org/10.1175/2010jpo4377.1

Hanson, J. L., & Phillips, O. M. (2001). Automated analysis of ocean surface directional wave spectra. *Journal of Atmospheric and Oceanic Technology*, *18*(2), 277–293. https://doi.org/10.1175/1520-0426(2001)018<0277:aaoosd>2.0.co;2

Hasselmann, K. (1962). On the non-linear energy transfer in a gravity-wave spectrum Part 1. General theory. *Journal of Fluid Mechanics*, *12*(4), 481–500. https://doi.org/10.1017/s0022112062000373

Hasselmann, K., Barnett, T., Bouws, E., Carlson, H., Cartwright, D., Enke, K., et al. (1973). *Measurements of wind-wave growth and swell decay during the joint North Sea wave project* (JONSWAP) (Tech. Rep.). Deutches Hydrographisches Institute.

Hasselmann, K., Chapron, B., Aouf, L., Ardhuin, F., Collard, F., Engen, G., et al. (2012). *The ERS SAR Wave Mode–a breakthrough in global ocean wave observations*. European Space Agency.

Hasselmann, S., Hasselmann, K., Allender, J. H., & Barnett, T. P. (1985). Computations and parameterizations of the nonlinear energy transfer in a gravity-wave specturm. Part II: Parameterizations of the nonlinear energy transfer for application in wave models. *Journal of Physical Oceanography*, *15*(11), 1378–1392. https://doi.org/10.1175/1520-0485(1985)015<1378:CAPOTN>2.0.CO;2

Hauser, D., Tourain, C., Hermozo, L., Alraddawi, D., Aouf, L., Chapron, B., et al. (2020). New observations from the SWIM radar on-board CFOSAT: Instrument validation and ocean wave measurement assessment. *IEEE Transactions on Geoscience and Remote Sensing*.

Hemer, M. A., Zieger, S., Durrant, T., O'Grady, J., Hoeke, R. K., McInnes, K. L., & Rosebrock, U. (2017). A revised assessment of Australia's national wave energy resource. *Renewable Energy*, *114*, 85–107. https://doi.org/10.1016/j.renene.2016.08.039

Hersbach, H., Bell, B., Berrisford, P., Hirahara, S., Horányi, A., Muñoz-Sabater, J., et al. (2020). The ERA5 global reanalysis. *Quarterly Journal of the Royal Meteorological Society*, *146*(730), 1999–2049. https://doi.org/10.1002/qj.3803

Huang, N. E., Long, S. R., Tung, C.-C., Yuen, Y., & Bliven, L. F. (1981). A unified two-parameter wave spectral model for a general sea state. *Journal of Fluid Mechanics*, *112*, 203–224. https://doi.org/10.1017/s0022112081000360

Hwang, P. A. (2011). A note on the ocean surface roughness spectrum. *Journal of Atmospheric and Oceanic Technology*, *28*(3), 436–443. https://doi.org/10.1175/2010JTECHO812.1

Janssen, P. A. E. M. (2003). Nonlinear four-wave interactions and freak waves. *Journal of Physical Oceanography*, *33*(4), 863–884. https://doi.org/10.1175/1520-0485(2003)33⟨863:NFIAFW⟩2.0.CO;2

Janssen, P. A. E. M. (2004). *The interaction of ocean waves and wind*. Cambridge University Press.

Janssen, P. A. E. M. (2008). Progress in ocean wave forecasting. *Journal of Computational Physics*, *227*(7), 3572–3594. https://doi.org/10.1016/j.jcp.2007.04.029

Janssen, P. A. E. M., & Bidlot, J.-R. (2009). *On the extension of the freak wave warning system and its verification* (Tech. Rep.). European Centre for Medium-Range Weather Forecasts.

Janssen, P. A. E. M., & Bidlot, J.-R. (2018). Progress in operational wave forecasting. *Procedia IUTAM*, *26*, 14–29. https://doi.org/10.1016/j.piutam.2018.03.003

Komen, G. J., Cavaleri, L., Donelan, M., Hasselmann, K., Hasselmann, S., & Janssen, P. (1994). *Dynamics and modelling of ocean waves*. Cambridge university press.

Kuik, A. J., van Vledder, G. P., & Holthuijsen, L. H. (1988). A method for the routine analysis of pitch-and-roll Buoy wave data. *Journal of Physical Oceanography*, *18*(7), 1020–1034. https://doi.org/10.1175/1520-0485(1988)018<1020:AMFTRA>2.0.CO;2

Lavergne, T., Sørensen, A. M., Kern, S., Tonboe, R., Notz, D., Aaboe, S., et al. (2019). Version 2 of the EUMETSAT OSI SAF and ESA CCI sea-ice concentration climate data records. *The Cryosphere*, *13*(1), 49–78. https://doi.org/10.5194/tc-13-49-2019

Li, J.-G. (2012). Propagation of ocean surface waves on a spherical multiple-cell grid. *Journal of Computational Physics*, *231*(24), 8262–8277. https://doi.org/10.1016/j.jcp.2012.08.007

Liu, Q., & Babanin, A. (2021). *Product user guide for the WW3-ST6 global wave hindcasts* (Tech. Rep.). University of Melbourne. https://doi.org/10.5281/zenodo.4497717

Liu, Q., Babanin, A. V., Fan, Y., Zieger, S., Guan, C., & Moon, I.-J. (2017). Numerical simulations of ocean surface waves under hurricane conditions: Assessment of existing model performance. *Ocean Modelling*, *118*, 73–93. https://doi.org/10.1016/j.ocemod.2017.08.005

Liu, Q., Babanin, A. V., Guan, C., Zieger, S., Sun, J., & Jia, Y. (2016). Calibration and validation of HY-2 altimeter wave height. *Journal of Atmospheric and Oceanic Technology*, *33*(5), 919–936. https://doi.org/10.1175/jtech-d-15-0219.1

Liu, Q., Gramstad, O., & Babanin, A. (2021). Kinetic equations in a third-generation spectral wave model. *Journal of Fluid Mechanics*, *910*, A50. https://doi.org/10.1017/jfm.2020.1036

Liu, Q., Rogers, W. E., Babanin, A., Li, J., & Guan, C. (2020). Spectral modeling of ice-induced wave decay. *Journal of Physical Oceanography*, *50*(6), 1583–1604. https://doi.org/10.1175/jpo-d-19-0187.1

Liu, Q., Rogers, W. E., Babanin, A. V., Young, I. R., Romero, L., Zieger, S., et al. (2019). Observation-based source terms in the third-generation wave model WAVEWATCH III: Updates and verification. *Journal of Physical Oceanography*, *49*(2), 489–517. https://doi.org/10.1175/jpo-d-18-0137.1

Masson, D. (1993). On the nonlinear coupling between swell and wind waves. *Journal of Physical Oceanography*, *23*(6), 1249–1258. https://doi.org/10.1175/1520-0485(1993)023<1249:otncbs>2.0.co;2

McAllister, M. L., Draycott, S., Adcock, T., Taylor, P., & Van Den Bremer, T. (2019). Laboratory recreation of the draupner wave and the role of breaking in crossing seas. *Journal of Fluid Mechanics*, *860*, 767–786. https://doi.org/10.1017/jfm.2018.886

McWilliams, J. C., Sullivan, P. P., & Moeng, C.-H. (1997). Langmuir turbulence in the ocean. *Journal of Fluid Mechanics*, *334*, 1–30. https://doi.org/10.1017/s0022112096004375

Meindl, E. A., & Hamilton, G. D. (1992). Programs of the national data buoy center. *Bulletin of the American Meteorological Society*, *73*(7), 985–993. https://doi.org/10.1175/1520-0477(1992)073<0985:potndb>2.0.co;2

Merchant, C. J., Embury, O., Bulgin, C. E., Block, T., Corlett, G. K., Fiedler, E., et al. (2019). Satellite-based time-series of sea-surface temperature since 1981 for climate applications. *Scientific data*, *6*(1), 1–18. https://doi.org/10.1038/s41597-019-0236-x

Meylan, M. H., Bennetts, L., Mosig, J., Rogers, W., Doble, M., & Peter, M. (2018). Dispersion relations, power laws, and energy loss for waves in the marginal ice zone. *Journal of Geophysical Research: Oceans*, *123*, 1–13. https://doi.org/10.1002/2018jc013776

Monin, A. S., & Obukhov, A. M. (1954). Basic laws of turbulent mixing in the surface layer of the atmosphere. *Proceedings of Geophysics Institute, National Academy of Science, SSSR*, *151*, 163–187.

Mori, N., Onorato, M., & Janssen, P. A. (2011). On the estimation of the kurtosis in directional sea states for freak wave forecasting. *Journal of Physical Oceanography*, *41*(8), 1484–1497. https://doi.org/10.1175/2011jpo4542.1

Onorato, M., Waseda, T., Toffoli, A., Cavaleri, L., Gramstad, O., Janssen, P., et al. (2009). Statistical properties of directional ocean waves: The role of the modulational instability in the formation of extreme events. *Physical Review Letters*, *102*(11), 114502. https://doi.org/10.1103/physrevlett.102.114502

Pereira, H. P. P., Violante-Carvalho, N., Nogueira, I. C. M., Babanin, A., Liu, Q., de Pinho, U. F., et al. (2017). Wave observations from an array of directional buoys over the southern brazilian coast. *Ocean Dynamics*, *67*(12), 1577–1591. https://doi.org/10.1007/s10236-017-1113-9

Qiao, F., Yuan, Y., Yang, Y., Zheng, Q., Xia, C., & Ma, J. (2004). Wave-induced mixing in the upper ocean: Distribution and application to a global ocean circulation model. *Geophysical Research Letters*, *31*(11), L11303. https://doi.org/10.1029/2004gl019824

Rapizo, H., Babanin, A., Provis, D., & Rogers, W. (2017). Current-induced dissipation in spectral wave models. *Journal of Geophysical Research: Oceans*, *122*(3), 2205–2225. https://doi.org/10.1002/2016jc012367

Rascle, N., & Ardhuin, F. (2013). A global wave parameter database for geophysical applications. Part 2: Model validation with improved source term parameterization. *Ocean Modelling*, *70*, 174–188. https://doi.org/10.1016/j.ocemod.2012.12.001

Rascle, N., Ardhuin, F., Queffeulou, P., & Croizé-Fillon, D. (2008). A global wave parameter database for geophysical applications. Part 1: Wave-current–turbulence interaction parameters for the open ocean based on traditional parameterizations. *Ocean Modelling*, *25*(3–4), 154–171. https://doi.org/10.1016/j.ocemod.2008.07.006

Rasmusson, E. M., & Carpenter, T. H. (1982). Variations in tropical sea surface temperature and surface wind fields associated with the southern oscillation/el niño. *Monthly Weather Review*, *110*(5), 354–384. https://doi.org/10.1175/1520-0493(1982)110<0354:vitsst>2.0.co;2

Resio, D. T., & Perrie, W. (2008). A two-scale approximation for efficient representation of nonlinear energy transfers in a wind wave spectrum. Part I: Theoretical development. *Journal of Physical Oceanography*, *38*(12), 2801–2816. https://doi.org/10.1175/2008jpo3713.1

Resio, D. T., Vincent, C. L., Tolman, H. L., Chawla, A., Rogers, W. E., Ardhuin, F., et al. (2019). *Progress during the nopp wave model improvement program*. arXiv. Retrieved from arXiv:1908.03601.

Ribal, A., Babanin, A. V., Young, I., Toffoli, A., & Stiassnie, M. (2013). Recurrent solutions of the alber equation initialized by joint north sea wave project spectra. *Journal of Fluid Mechanics*, *719*, 314–344. https://doi.org/10.1017/jfm.2013.7

Ribal, A., Babanin, A. V., Zieger, S., & Liu, Q. (2020). A high-resolution wave energy resource assessment of Indonesia. *Renewable Energy*, *160*, 1349–1363. https://doi.org/10.1016/j.renene.2020.06.017

Ribal, A., & Young, I. R. (2019). 33 years of globally calibrated wave height and wind speed data based on altimeter observations. *Scientific data*, *6*(1), 1–15. https://doi.org/10.1038/s41597-019-0108-4

Rogers, W. E. (2017). Mean square slope in SWAN and WAVEWATCH III; buoy response functions; and limitations of ST1 physics in SWAN. In *Waves in shallow water environments meeting (wise-24)*. Canada. Retrieved from https://www7320.nrlssc.navy.mil/dynamic/posters/rogers.afterWISE2017.pdf

Rogers, W. E., Babanin, A. V., & Wang, D. W. (2012). Observation-consistent input and whitecapping dissipation in a model for wind-generated surface waves: Description and simple calculations. *Journal of Atmospheric and Oceanic Technology*, *29*(9), 1329–1346. https://doi.org/10.1175/JTECH-D-11-00092.1

Rogers, W. E., & Campbell, T. J. (2009). *Implementation of curvilinear coordinate system in the WAVEWATCH III model* (Tech. Rep.). Naval Research Laboratory.

Rogers, W. E., & Linzell, R. S. (2018). *The IRI grid system for use with WAVEWATCH III* (Tech. Rep.). Naval Research Laboratory. Retrieved from https://www7320.nrlssc.navy.mil/pubs/2018/rogers8-2018.pdf

Rogers, W. E., Thomson, J., Shen, H. H., Doble, M. J., Wadhams, P., & Cheng, S. (2016). Dissipation of wind waves by pancake and frazil ice in the autumn Beaufort Sea. *Journal of Geophysical Research: Oceans*, *121*(11), 7991–8007. https://doi.org/10.1002/2016jc012251

Rogers, W. E., & van Vledder, G. P. (2013). Frequency width in predictions of windsea spectra and the role of the nonlinear solver. *Ocean Modelling*, *70*, 52–61. https://doi.org/10.1016/j.ocemod.2012.11.010

Roland, A. (2008). *Development of wwm ii: Spectral wave modelling on unstructured meshes* (Unpublished doctoral dissertation). Technische Universität Darmstadt.

Romero, L. (2019). Distribution of surface wave breaking fronts. *Geophysical Research Letters*, *46*(17–18), 10463–10474. https://doi.org/10.1029/2019gl083408

Saha, S., Moorthi, S., Pan, H.-L., Wu, X., Wang, J., Nadiga, S., et al. (2010). The NCEP climate forecast system reanalysis. *Bulletin of the American Meteorological Society*, *91*(8), 1015–1058. https://doi.org/10.1175/2010BAMS3001.1

Saha, S., Moorthi, S., Wu, X., Wang, J., Nadiga, S., Tripp, P., et al. (2014). The NCEP climate forecast system version 2. *Journal of Climate*, *27*(6), 2185–2208. https://doi.org/10.1175/JCLI-D-12-00823.1

Salisbury, D. J., Anguelova, M. D., & Brooks, I. M. (2014). Global distribution and seasonal dependence of satellite-based whitecap fraction. *Geophysical Research Letters*, *41*(5), 1616–1623. https://doi.org/10.1002/2014gl059246

Semedo, A., Sušelj, K., Rutgersson, A., & Sterl, A. (2011). A global view on the wind sea and swell climate and variability from era-40. *Journal of Climate*, *24*(5), 1461–1479. https://doi.org/10.1175/2010jcli3718.1

Seymour, R. J., Sessions, M. H., & Castel, D. (1985). Automated remote recording and analysis of coastal data. *Journal of Waterway, Port, Coastal, and Ocean Engineering*, *111*(2), 388–400. https://doi.org/10.1061/(asce)0733-950x(1985)111:2(388)

Sharqawy, M. H., Lienhard, J. H., & Zubair, S. M. (2010). Thermophysical properties of seawater: A review of existing correlations and data. *Desalination and water Treatment*, *16*(1–3), 354–380. https://doi.org/10.5004/dwt.2010.1079

Smit, P. B., & Janssen, T. T. (2019). Swell propagation through submesoscale turbulence. *Journal of Physical Oceanography*, *49*(10), 2615–2630. https://doi.org/10.1175/jpo-d-18-0250.1

Snodgrass, F., Hasselmann, K., Miller, G., Munk, W. H., & Powers, W. (1966). Propagation of ocean swell across the pacific. *Philosophical Transactions of the Royal Society of London - Series A: Mathematical and Physical Sciences*, *259*(1103), 431–497. https://doi.org/10.1098/rsta.1966.0022

Squire, V. A. (2019). Ocean wave interactions with sea ice: A 2019 reappraisal. *Annual Review of Fluid Mechanics*, *52*, 37–60. https://doi.org/10.1146/annurev-fluid-010719-060301

Stopa, J. E., Ardhuin, F., Babanin, A., & Zieger, S. (2016). Comparison and validation of physical wave parameterizations in spectral wave models. *Ocean Modelling*, *103*, 2–17. https://doi.org/10.1016/j.ocemod.2015.09.003

Stopa, J. E., & Cheung, K. F. (2014). Intercomparison of wind and wave data from the ECMWF reanalysis interim and the NCEP climate forecast system reanalysis. *Ocean Modelling*, *75*, 65–83. https://doi.org/10.1016/j.ocemod.2013.12.006

The WAMDI Group. (1988). The WAM model-A third generation ocean wave prediction model. *Journal of Physical Oceanography*, *18*(12), 1775–1810.

The WAVEWATCH III Development Group (WW3DG) (2019). *User manual and system documentation of WAVEWATCH III® version 6.07* (Tech. Note No. 333) (p. 465). NOAA/NWS/NCEP/MMAB.

Thomson, J., Schwendeman, M. S., Zippel, S. F., Moghimi, S., Gemmrich, J., & Rogers, W. E. (2016). Wave-breaking turbulence in the ocean surface layer. *Journal of Physical Oceanography*, *46*(6), 1857–1870. https://doi.org/10.1175/jpo-d-15-0130.1

Timmermans, B., Gommenginger, C., Dodet, G., & Bidlot, J.-R. (2020). Global wave height trends and variability from new multimission satellite altimeter products, reanalyses, and wave buoys. *Geophysical Research Letters*, *47*(9), e2019GL086880. https://doi.org/10.1029/2019gl086880

Toffoli, A., Bitner-Gregersen, E., Osborne, A. R., Serio, M., Monbaliu, J., & Onorato, M. (2011). Extreme waves in random crossing seas: Laboratory experiments and numerical simulations. *Geophysical Research Letters*, *38*(6), L06605. https://doi.org/10.1029/2011gl046827

Tolman, H. L. (1991). A third-generation model for wind waves on slowly varying, unsteady, and inhomogeneous depths and currents. *Journal of Physical Oceanography*, *21*(6), 782–797. https://doi.org/10.1175/1520-0485(1991)021<0782:atgmfw>2.0.co;2

Tolman, H. L. (2002). Alleviating the garden sprinkler effect in wind wave models. *Ocean Modelling*, *4*(3–4), 269–289. https://doi.org/10.1016/s1463-5003(02)00004-5

Tolman, H. L. (2003). Treatment of unresolved islands and ice in wind wave models. *Ocean Modelling*, *5*(3), 219–231. https://doi.org/10.1016/S1463-5003(02)00040-9

Tolman, H. L. (2013). A generalized multiple discrete interaction approximation for resonant four-wave interactions in wind wave models. *Ocean Modelling*, *70*, 11–24. https://doi.org/10.1016/j.ocemod.2013.02.005

Tracy, B., Devaliere, E.-M., Nicolini, T., Tolman, H. L., & Hanson, J. L. (2007). Wind sea and swell delineation for numerical wave modeling. In 10th international workshop on wave hincasting and forecasting & coastal hazards symposium, JCOMM Technical Report 41 WMO/TD-No. 1442 (Paper P12).

Trowbridge, J., Weller, R., Kelley, D., Dever, E., Plueddemann, A., Barth, J. A., & Kawka, O. (2019). The ocean observatories initiative. *Frontiers in Marine Science*, *6*, 74. https://doi.org/10.3389/fmars.2019.00074

Tsagareli, K. N., Babanin, A. V., Walker, D. J., & Young, I. R. (2010). Numerical investigation of spectral evolution of wind waves. Part I: Wind-input source function. *Journal of Physical Oceanography*, *40*(4), 656–666. https://doi.org/10.1175/2009JPO4345.1

Tulin, M. P., & Waseda, T. (1999). Laboratory observations of wave group evolution, including breaking effects. *Journal of Fluid Mechanics*, *378*, 197–232. https://doi.org/10.1017/s0022112098003255

van Vledder, G. P., Hulst, S. T. C., & McConochie, J. D. (2016). Source term balance in a severe storm in the southern north sea. *Ocean Dynamics*, *66*(12), 1681–1697. https://doi.org/10.1007/s10236-016-0998-z

Voermans, J., Babanin, A., Thomson, J., Smith, M., & Shen, H. (2019). Wave attenuation by sea ice turbulence. *Geophysical Research Letters*, *5*, 6796–6803. https://doi.org/10.1029/2019GL082945

Wang, J., Li, B., Gao, Z., & Wang, J. (2019). Comparison of ECMWF significant wave height forecasts in the china sea with buoy data. *Weather and Forecasting*, *34*(6), 1693–1704. https://doi.org/10.1175/waf-d-19-0043.1

Williams, T. D., Bennetts, L. G., Squire, V. A., Dumont, D., & Bertino, L. (2013). Wave-ice interactions in the marginal ice zone. Part 1: Theoretical foundations. *Ocean Modelling*, *71*, 81–91. https://doi.org/10.1016/j.ocemod.2013.05.010

Young, I. R. (1993). An estimate of the Geosat altimeter wind speed algorithm at high wind speeds. *Journal of Geophysical Research*, *98*(C11), 20275–20285. https://doi.org/10.1029/93jc02117

Young, I. R. (1999a). Seasonal variability of the global ocean wind and wave climate. *International Journal of Climatology: A Journal of the Royal Meteorological Society*, *19*(9), 931–950. https://doi.org/10.1002/(sici)1097-0088(199907)19:9<931::aid-joc412>3.0.co;2-o

Young, I. R. (1999b). *Wind generated ocean waves*. Elsevier Science Ltd.

Young, I. R., & Babanin, A. V. (2006). Spectral distribution of energy dissipation of wind-generated waves due to dominant wave breaking. *Journal of Physical Oceanography*, *36*(3), 376–394. https://doi.org/10.1175/jpo2859.1

Young, I. R., & Donelan, M. (2018). On the determination of global ocean wind and wave climate from satellite observations. *Remote Sensing of Environment*, *215*, 228–241. https://doi.org/10.1016/j.rse.2018.06.006

Young, I. R., Fontaine, E., Liu, Q., & Babanin, A. V. (2020). The wave climate of the Southern Ocean. *Journal of Physical Oceanography*, *50*(5), 1417–1433. https://doi.org/10.1175/JPO-D-20-003110.1175/JPO-D-20-0031.110.1175/jpo-d-20-0031.1

Young, I. R., & Verhagen, L. (1996). The growth of fetch limited waves in water of finite depth. Part 2. Spectral evolution. *Coastal Engineering*, *29*(1–2), 79–99. https://doi.org/10.1016/s0378-3839(96)00007-5

Zieger, S., Babanin, A. V., Rogers, W. E., & Young, I. R. (2015). Observation-based source terms in the third-generation wave model WAVE-WATCH. *Ocean Modelling*, *218*, 1–25. https://doi.org/10.1016/j.ocemod.2015.07.014

Zieger, S., Vinoth, J., & Young, I. R. (2009). Joint calibration of multiplatform altimeter measurements of wind speed and wave height over the past 20 Years. *Journal of Atmospheric and Oceanic Technology*, *26*(12), 2549–2564. https://doi.org/10.1175/2009JTECHA1303.1

Zijlema, M., Van Vledder, G. P., & Holthuijsen, L. (2012). Bottom friction and wind drag for wave models. *Coastal Engineering*, *65*, 19–26. https://doi.org/10.1016/j.coastaleng.2012.03.002